Symmetry-enforced topological phononic quadratic Dirac points, type-III nodal rings, and nodal surfaces in $BaNa_2$

Jiaxi Liu,[1,2] Peitao Liu,[2] Yan Sun,[2] Xing-Qiu Chen,[2,*] and Jiangxu Li[2,†]

[1]*School of Materials Science and Engineering, University of Science and Technology of China, Shenyang 110016, China*

[2]*Shenyang National Laboratory for Materials Science, Institute of Metal Research, Chinese Academy of Sciences, Shenyang 110016, China*

(Received 4 January 2023; revised 21 March 2023; accepted 7 September 2023; published 15 September 2023)

Topological gapless phonons have been extensively studied both in crystal symmetry and materials realization due to their spinless properties. Based on degeneracy and geometry, they can be categorized into the topological nodal point, line, and surface as well as other complex topological phonons. However, the coexistence of more than two types of topological phonons in a single material is rarely reported due to strict symmetry constraints. By means of symmetry analysis, $k \cdot p$ model, and first-principles calculations, we found that the quadratic Dirac point (QDP), type-III nodal ring (NR), and nodal surface (NS) can simultaneously emerge under the symmetry protection of space group $P6_3/mmc$. We also predicted a series of candidate materials for experimental realizations. As a representative, we performed a thorough investigation of $BaNa_2$ in the C14 Laves phase, analyzing its bulk phonon dispersion relationships, topological invariants, and topological surface states. We unveiled the underlying mechanism for the coexistence of QDPs, NRs, and NSs. This study not only highlights the significance of crystal symmetry in realizing novel topological phonons but also lays the foundation for the analysis of topological materials with hybrid topological characteristics.

DOI: 10.1103/PhysRevB.108.104312

I. INTRODUCTION

Topological quantum states of matter [1–3] are important topics in condensed matter physics and materials science. Numerous topological electronic materials [4–8], including topological insulators [9–12], Dirac/Weyl semimetals [13–17], and nodal line semimetals [18–21], have been theoretically proposed, with some already experimentally verified. Due to their unique physical mechanisms and promising device applications, topological electronic materials have received considerable attention. Phonons [22], the most basic emergent boson of the crystalline lattice, are a type of energy carrier and are closely correlated to thermal conductivity and specific heat. Analogous to well-studied electronic systems, topological concepts have been extended to the field of phonons as topological phonons (TPs). Unlike electrons, phonons are bosons and obey the Bose-Einstein statistics. Consequently, they can be experimentally detected throughout the entire energy range. Nowadays, numerous types of TPs have been theoretically predicted in real solid-state materials. Using symmetry analysis, Yu *et al.* [23] conducted a systematic study on the emergent particles in three-dimensional crystals, providing a comprehensive understanding of all possible novel particles in physical systems.

Based on the band crossing dimensions, TPs [23–27] can be broadly classified into three types: (i) zero-dimensional (0D) nodal points [28–33], including topological Weyl phonons [34–45] and Dirac phonons [46,47]; (ii) one-dimensional (1D) nodal lines [48–51], including the nodal straight lines [52–54], nodal rings [55–63], and complex nodal lines such as nodal link [64], nodal chain [65–68], nodal net [68,69], and nodal cage [70,71]; and (iii) two-dimensional (2D) nodal surfaces [72–76]. Each type of TPs has been predicted in different materials and the coexistences of TPs have also been reported in materials with varying dimensions [23,25,51,68]. For instance, triply degenerate points, Dirac points, and Weyl nodal lines have been observed in SnO_2 [28]. For the AgZr alloy, hybrid-type nodal ring and higher-order quadratic nodal line phonons are found [58]. In the high-pressure phase of CuCl [64], topological phononic nodal hexahedron net and nodal links are observed. However, to the best of our knowledge, the coexistence of three types of TPs, particularly, 0D quadratic Dirac point (QDP), 1D type-III nodal ring (NR), and 2D nodal surface (NS) has rarely been reported owing to strict symmetry constraints.

In this regard, symmetry analysis enables us to investigate the types of materials capable of hosting topological phonons in three distinct dimensions. Here, by a combination of symmetry analysis, $k \cdot p$ model [4,23,57,77–79], and first-principles calculations, we systematically investigated TPs in the hexagonal space group (SG) $P6_3/mmc$ (No. 194), providing a comprehensive understanding of the coexistence of 0D QDPs, 1D type-III NRs, and 2D NSs, which are protected by the inversion symmetry ($\mathcal{P}$), time-reversal symmetry ($\mathcal{T}$), mirror symmetry ($\tilde{M}_z$), and screw symmetry ($\mathcal{S}$).

This paper is organized as follows. In Sec. II A, we give a symmetry analysis of QDPs, type-III NRs, and NSs. The details of our first-principles methods are presented in Sec. II B. In Sec. III, we take $BaNa_2$ as a representative to present our results, including the phonon spectrum of $BaNa_2$ (Sec. III A), group theory analysis, and $k \cdot p$ model derivation for QDPs (Sec. III B), type-III NRs (Sec. III C), and NSs (Sec. III D).

*xingqiu.chen@imr.ac.cn
†jxli15s@imr.ac.cn

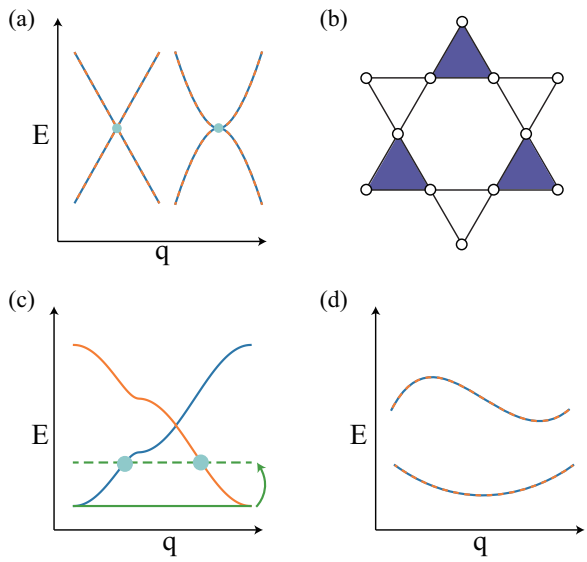

FIG. 1. (a) Typical band structures of the Dirac point and quadratic Dirac point in 3D crystals. (b) A 2D kagome lattice and (c) the corresponding band structure. The arrow in panel (c) denotes the change in the position of the flat band by varying the hopping parameters. Note that the existence of the flat band (green line) is required for the appearance of the type-III nodal ring (solid circles). (d) Schematic band structure of the nodal surface, where all the points on one reciprocal plane are twofold degenerate.

Section III E provides evidence for the emergence of nontrivial surface states induced by the topological phases. Finally, we summarize the key findings and present closing remarks in Sec. IV.

II. SYMMETRY ANALYSIS AND COMPUTATIONAL DETAILS

A. Symmetry analysis

Let us first analyze the symmetry properties of SG $P6_3/mmc$ to elucidate the underlying mechanism for QDPs, type-III NRs, and NSs, respectively. Realizing these three topological phases requires different degeneracies of phonon branches. The nontrivial crossing points of these branches are protected by specific crystal symmetries, which prevent the presence of perturbation terms that could open up a gap [46]. Based on the irreducible representations (IRs) and symmetry constraints, we investigate fourfold degeneracy at high-symmetry points (HSPs) for QDPs, as well as the twofold degeneracy at high-symmetry planes for type-III NRs and NSs, respectively.

First, we aim to study the QDPs at HSPs. Dirac phonons exhibit a fourfold degeneracy and can be viewed as consisting of two Weyl points with opposite chirality. From the dispersion, Dirac phonons can be categorized into two types: (1) Dirac phonons with linear dispersion along all directions in the 3D momentum space, as illustrated in the left panel of Fig. 1(a), which follows the massless Dirac equation. (2) Dirac points with quadratic dispersions, termed as QDPs, owing to the dominance of second-order terms in the Hamiltonian. The QDPs are more commonly found in phonon spectrum of real materials and is visually represented on the right of Fig. 1(a). Under the $\mathcal{T}$ symmetry, SG $P6_3/mmc$ possesses four-dimensional (4D) IR at A (0.0, 0.0, 0.5), where the QDPs can be expected under the protection of nonsymmorphic symmetry. Notably, the topological charge of QDP is 0 due to the presence of the $\mathcal{PT}$ symmetry.

Next, we elucidate the protected mechanism of type-III NRs. In general, the NRs can be protected by the $\mathcal{PT}$ symmetry, which requires the Berry phase along any closed path circling the ring crossings must be quantized in units of π, preventing any gap opening by weak perturbations that preserve the $\mathcal{PT}$ symmetry. Once the ring splits, the Berry phase deviates from the quantized π, thus breaking the topological protections provided by $\mathcal{PT}$ symmetry [80,81]. Furthermore, additional crystal symmetry, such as mirror or rotation symmetries, can constrain NRs into high-symmetry lines or planes. Here, we employ a simplified Hamiltonian to exemplify this phenomenon. As for a general NR in a mirror plane, one possible two-band Hamiltonian [55–57] can be expressed as

$$H(\mathbf{q}) = t_0 q_+ q_- \sigma_0 + t_1\left(q_+ q_- - r_0^2\right)\sigma_x + t_2 q_z \sigma_z,$$

where q_i, $i = x, y, z$ are components of the reciprocal vector $\mathbf{q}$, $q_\pm = q_x \pm i q_y$, and t_i, $i = 0, 1, 2$ are three real coefficients, σ_0 is the identity matrix, and σ_x and σ_z are two Pauli matrices. The first term represents a tilt of the spectrum. The energy of the two branches should be

$$\epsilon_\pm = T(\mathbf{q}) \pm U(\mathbf{q}) = t_0 q_+ q_- \pm \sqrt{t_1^2\left(q_+ q_- - r_0^2\right)^2 + t_2^2 q_z^2},$$

where $T(\mathbf{q})$ and $U(\mathbf{q})$ can be considered as the kinetic and potential components of the energy spectrum. The low-energy model describes a NR with a radius of r_0 in the $q_z = 0$ plane, which is protected by mirror symmetry $\mathcal{M}_z$. In the q_x-q_y plane, a flat band emerges when the kinetic energy $T(\mathbf{q})$ equals the potential energy $U(\mathbf{q})$ at a critical condition ($t_0/t_1 = 1$), which can also lead to the formation of the type-III nodal ring [57]. As shown in Figs. 1(b) and 1(c), SG $P6_3/mmc$ possesses sixfold rotation symmetry and mirror symmetry, enabling it to provide both triangular and kagome planes that can create a perfectly flat band in the entire Brillouin zone (BZ). The shift of the flat band results in the emergence of a type-III nodal ring with opposite mirror eigenvalues (see more details in Appendix A).

After investigating the 0D QDPs and 1D NRs, we now focus on the symmetry analysis of 2D NSs formed by band crossings. The simultaneous occurrence of twofold degeneracy for all points on a BZ plane leads to the formation of the topological NS [4], as illustrated in Fig. 1(d). Each point on the surface is a crossing point between two bands, hosting the linear dispersion along the surface normal direction. For SG $P6_3/mmc$, the combination of screw symmetry $\mathcal{S}$ and time-reversal symmetry $\mathcal{T}$ results in a Kramers' degeneracy condition on the plane at the BZ boundary. This guarantees the emergence of the NS belonging to class-II NS, whose presence and location solely depend on the symmetries.

Based on the above analysis, we obtained that SG $P6_3/mmc$ has the potential to facilitate the emergence of all three types of topological phonons. Furthermore, we employed a high-throughput screening strategy using our topological phonon database [25,26] to realize the data-driven design of topological phonons and predicted numerous can-

didate materials. In the following, the $BaNa_2$ served as a prototype to demonstrate the coexistence of QDPs, type-III NRs, and NSs.

B. Computational details

The first-principles calculations were performed using the Vienna *ab initio* simulation package (VASP) [82–84] based on the density functional theory (DFT) [85,86]. For the exchange-correlation function, we adopted the generalized gradient approximation (GGA) in the form of the Perdew-Burke-Ernzerhof function (PBE) [87–89], which treats semi-core valence electrons as valence electrons. A self-consistent field method (tolerance 10^{-5} eV per unit cell) was employed in conjunction with plane wave basis sets with a cutoff energy of 550 eV. Atomic structure optimization was implemented until the remanent Hellmann-Feynman forces on the ions were less than 0.0001 eV/Å. A Γ-centered $11\times11\times7$ k-mesh was used to sample the BZ. Achieving stable phonon spectra requires precise optimization of lattice constants by minimizing the interionic forces to less than 0.0001 eV/Å. The force constants were computed using the Phonopy package [90,91] based on the density functional perturbation theory (DFPT) [92]. We employed a $2\times2\times1$ supercell with 48 atoms, which was sufficiently large for describing the forces, to determine the force constants. Dynamic matrices were then constructed using stable second-order force constants as tight-binding parameters. The surface density of states (DOS) was obtained by surface iteration Green's function method [93] embedded in TPHONON, and $k\cdot p$ model parameters were estimated using particle swarm optimization (PSO).

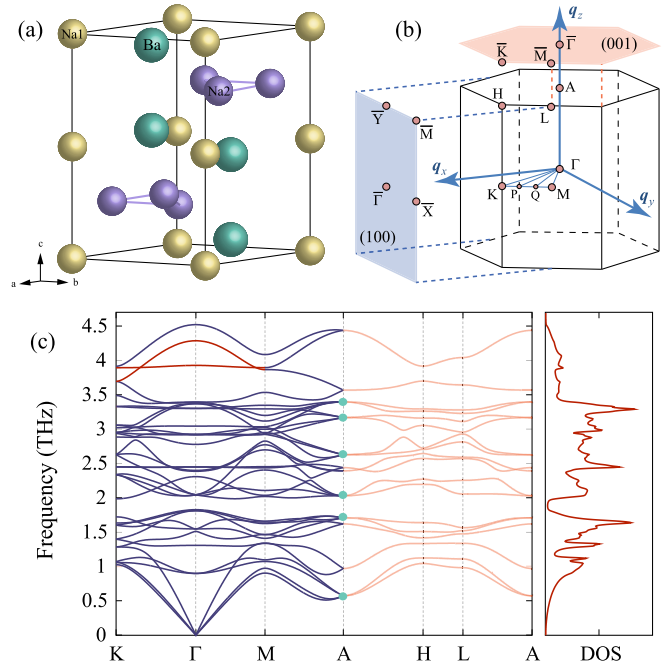

FIG. 2. (a) Crystal structure of $BaNa_2$, in which the green, yellow, and purple spheres represent Ba, Na1, and Na2 atoms, respectively. (b) Bulk BZ and surface BZs for the (0001) and (10$\bar{1}$0) surfaces. The corresponding HSPs are marked by circles. (c) Phonon band structure along the high-symmetry lines and phonon density of states. The orange lines are twofold degenerate nodal lines, the red lines represent the flat nodal ring, and the solid green circles denote quadratic Dirac points.

III. RESULTS AND DISCUSSIONS

A. Structure and phononic band crossing points

The structure of $BaNa_2$ is displayed in Fig. 2(a), which belongs to the nonsymmorphic SG $P6_3/mmc$. The primitive cell of $BaNa_2$ contains 12 atoms, with all Ba atoms occupying the $4f$ position $(1/3, 2/3, u)$ with $u = 0.439$ in an ABAB stacking, while Na atoms occupying $2a$ position (0, 0, 0) and $6h$ position $(x, 2x, 1/4)$ with $x = 0.169$. As shown in Figs. 2(a) and 7 of the Appendix, the Na2 atoms form the kagome lattice, while the Na1 atoms form a 2D triangular lattice. The atomic layers of Na1 and Na2 can assemble into a hexahedron structure enclosing the Ba atoms. The optimized lattice parameters are $a = b = 7.301$ Å and $c = 11.841$ Å, which are in good agreement with experimental values [94] of $a = b = 7.393$ Å and $c = 11.999$ Å. Figure 2(b) shows both the bulk and surface Brillouin zones, where the orange and light-blue planes represent the projections of (0001) and (10$\bar{1}$0) surfaces, respectively. On the (0001) surface, Γ (A), M (L), and K (H) are projected onto Γ, $\bar{M}$, and $\bar{K}$, respectively. On the (10$\bar{1}$0) surface, Γ, M, L, and A are projected onto $\bar{\Gamma}$, $\bar{X}$, $\bar{M}$, and $\bar{Y}$, respectively. The phonon bands along high-symmetry paths and the phonon DOS are shown in Fig. 2(c). Clearly, all branches have no imaginary frequencies throughout the whole BZ, verifying the dynamical stability of $BaNa_2$. As shown in Fig. 2(c), the little group of high-symmetry point A has three distinct IRs noted as A_1^2, A_2^2, and A_3^4. All phonon branches should be degenerate at A with twofold or fourfold degeneracy. In total, there are six QDPs represented by solid green circles with IRs of A_3^4. At approximately 3.93 THz, we observe a flat phonon branch that forms a type-III nodal ring represented by the red lines. Moreover, the twofold degeneracy of all bands along the A-H-L-A path, represented by the orange lines, indicates the existence of NS in the $q_z = \pi$ plane. In the following, based on the DFT results, we systematically investigate the QDPs, type-III NRs and NSs by detailed symmetry analysis and $k\cdot p$ models.

B. Quadratic Dirac points

We begin by investigating the QDPs located at the high-symmetry point A $(0, 0, 0.5)$. Multifold crossings at high-symmetry points commonly exhibit nonlinear dispersion, whereas the phonon crossings with linear dispersion can be expected at general $\mathbf{q}$-points. The nonsymmorphic symmetries can protect the nontrivial crossings with fourfold degeneracy from perturbations. Since phonons are bosonic systems, we need to analyze the single-valued representations of A with time-reversal symmetry ($\mathcal{T}^2 = 1$). According to Ref. [95], the abstract group of the high-symmetry point A in SG $P6_3/mmc$ belongs to G_{48}^1 with three generating elements including sixfold screw symmetry ($\mathcal{S}_{6z} = \{C_6^+|00\frac{1}{2}\}$), twofold rotation symmetry ($C_{21}'' = \{C_{2,110}|000\}$), and space inversion symmetry ($\mathcal{P} = \{\mathcal{I}|000\}$). Both 2D IRs ($A_1^2$ and A_2^2) and 4D IR (A_3^4) are responsible for the degeneracy of phonon branches. The 4D IR A_3^4 indicates the existence of QDPs.

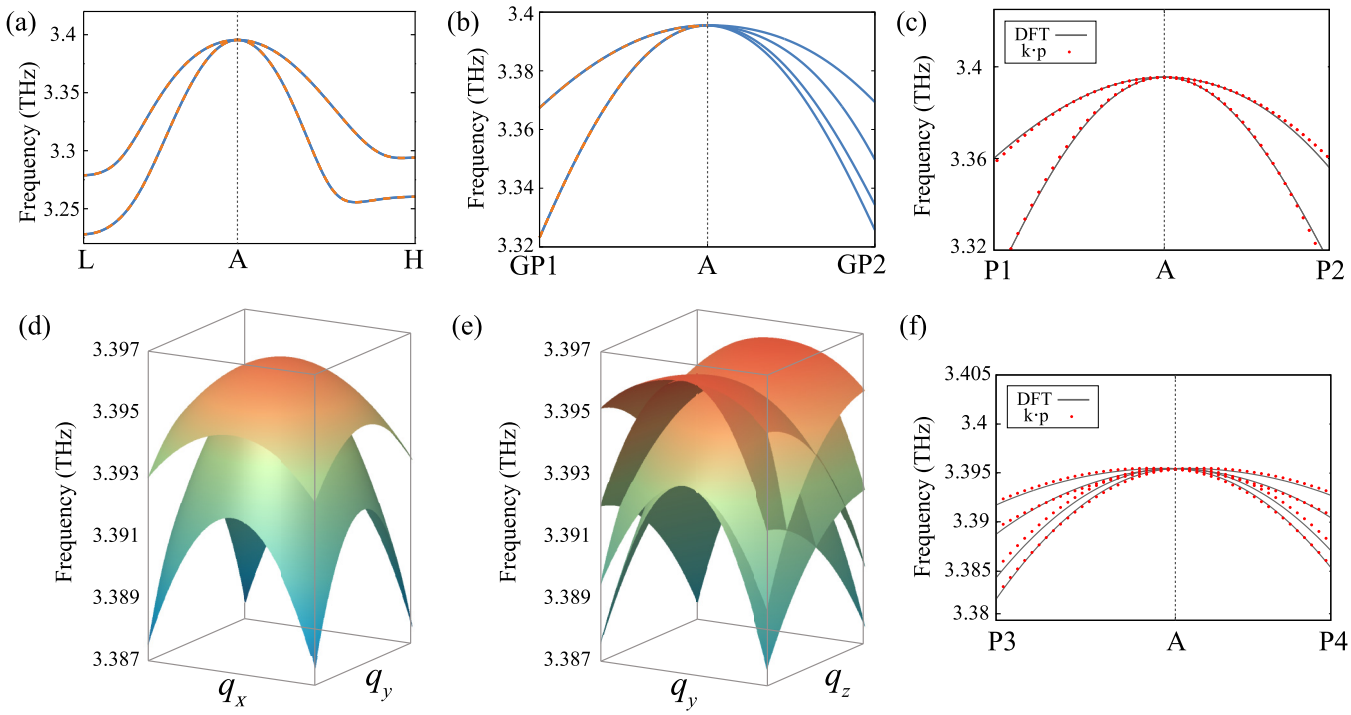

FIG. 3. (a), (b) Phonon dispersions around QDP along different paths, in which GP1 at (0.12, 0.12, 0.5) and GP2 at (0.2, 0.0, 0.4) are off the high-symmetry momentum path. (c), (f) Comparison between DFT bands and bands from the $k \cdot p$ model around QDP along different paths, and P1–P4 are the general points on each path. The dark gray lines correspond to DFT calculations, and the red dots correspond to the $k \cdot p$ model. (c) Phonon dispersion along the high-symmetry path in the $q_z = \pi$ plane. (f) Phonon dispersion along a general path out of the $q_z = \pi$ plane. (d) Phonon dispersion around the QDP on the q_x-q_y plane. (e) Phonon dispersion around the QDP on the q_y-q_z plane. All dispersions in panels (d) and (e) are calculated within a range of 0.015 Å^{-1}.

To analyze the feature of QDPs at A, we derived a four-band model for $BaNa_2$. For A in the hexagonal lattice, the sixfold screw symmetry can generate the elements in the little group. The transformation of the lattice coordinates under $\mathcal{S}_{6z}$ is given by

$$\mathcal{S}_{6z} : (x, y, z) \longrightarrow (x - y, x, z + 1/2).$$

As a result, $\mathcal{S}_{6z}^6$ produces an integer lattice translation along the $(0, 0, q_z)$ axis:

$$\mathcal{S}_{6z}^6 = e^{-iq_z \cdot 3c},$$

here, c is the lattice constant. $\mathcal{S}_{6z} = \{C_6^+ | 00\frac{1}{2}\}$, where C_6^+ denotes the sixfold rotation operator. The eigenvalues of $\mathcal{S}_{6z}$ can be expressed as $E_n = e^{i2\pi n/6} \cdot e^{-iq_z \cdot c/2}$ $(n = 0, 1, \ldots, 5)$ (see Appendix B). To construct the four-band effective $k \cdot p$ model, we need to identify four linearly independent basis functions from six eigenstates of $\mathcal{S}_{6z}$. From the table of abstract group G_{48}^1, we can obtain the following relations:

$$(\mathcal{S}_{6z})^{12} = (C_{21}'')^2 = \mathcal{I}^2 = E, \quad (1)$$

$$(\mathcal{S}_{6z})^{11} C_{21}'' = C_{21}'' \mathcal{S}_{6z}, \quad (2)$$

$$(\mathcal{S}_{6z})^7 \mathcal{I} = \mathcal{I} \mathcal{S}_{6z}. \quad (3)$$

Based on those relations, we derived the anticommutation and commutation relations of the operators for A as follows:

$$\{\mathcal{S}_{6z}, \mathcal{I}\} = 0, \quad [C_{21}'', \mathcal{I}] = 0.$$

Considering $\mathcal{T}$ symmetry, we started from the eigenstates $|e^{\pm i\frac{\pi}{6}}\rangle$ and $|e^{\pm i\frac{5\pi}{6}}\rangle$ to simplify the effective model. The representation of $\mathcal{S}_{6z}$ is given by the diagonal matrix $\mathrm{diag}\{e^{i\frac{\pi}{6}}, e^{-i\frac{5\pi}{6}}, e^{-i\frac{\pi}{6}}, e^{i\frac{5\pi}{6}}\}$. The matrix representations of the other two generators are $C_{21}'' = \sigma_1 \otimes \sigma_0$ and $\mathcal{I} = \sigma_0 \otimes \sigma_1$, where σ_1 is the Pauli matrix, and σ_0 is the 2×2 identity matrix. $\mathcal{T}$ is represented by $\mathcal{T} = \sigma_1 \otimes \sigma_0 \mathcal{K}$, where $\mathcal{K}$ is the complex conjugate operator. These four states form a complete orthonormal basis to represent the 4D IR.

The effective $k \cdot p$ Hamiltonian can be generated from the above four operators as follows:

$$\begin{aligned}\mathcal{H}_{\mathrm{eff}}(\mathbf{q}) = &\left[E_0 + t_1 q_+ q_- + t_2 q_z^2\right] + t_3 q_z \sigma_3 \sigma_3 \\ &+ t_4 q_z [(q_x + q_y)\sigma_2 - (q_x - q_y)\sigma_1]\sigma_0 \\ &+ t_5 [q_-^2 (i\sigma_1 - \sigma_2) - q_+^2 (i\sigma_1 + \sigma_2)]\sigma_1, \end{aligned} \quad (4)$$

where $\sigma_{1,2,3}$ are three Pauli matrices, $q_\pm = q_x \pm i q_y$ and $q_{x,y,z}$ are momenta away from A, and E_0 and t_n are real coefficients $(n \in [1, 5])$. Based on the above analysis, the 2D and 4D IRs at A point yield two types of degenerate phonon branches as shown in Fig. 2(c). Six QDPs are represented by solid green circles in the whole frequency range. The 4D IR of A guarantees the fourfold degeneracy.

To fit model parameters, we focused on the QDP at 3.396 THz. Figure 3 demonstrates phonon bands along different paths and planes centered at A. We first concentrate on the L-A-H path located in the $q_z = \pi$ plane displayed in Fig. 3(a). The two bands that correspond to twofold degenerate branches

TABLE I. $k \cdot p$ model parameters for QDPs.

Phonon branches	1–4	9–12	13–16	21–24	25–28	29–32
E_0(THz)	0.572	1.708	2.028	2.625	3.168	3.396
t_1(THzÅ^2)	3.800	−1.20	3.600	0.400	−0.04	−1.19
t_2(THzÅ^2)	12.80	14.00	−1.20	0.200	0.100	0.040
t_3(THzÅ)	1.900	0.700	0.180	1.050	0.800	0.060
t_4(THzÅ^2)	0.160	0.160	0.160	0.160	0.160	0.160
t_5(THzÅ^2)	−0.60	0.800	3.000	0.300	0.450	0.500

are indicated by orange dotted and blue solid lines, respectively. The dispersion has the shape of a Mexican hat. Two doubly degenerate phonon bands merge at point A, as dictated by the 4D IR. Figure 3(d) shows that both of them are twofold degenerate on the q_x-q_y plane, confirming the existence of a nodal surface on the $q_z = \pi$ plane. To investigate the phonon dispersion beyond the high-symmetry line and the $q_z = \pi$ plane, we plot the phonon bands along GP1-A-GP2 for the general path presented in Fig. 3(b). The phonon bands retain a twofold degeneracy throughout GP1-A, and they will split into two individual branches along the path A-GP2. The screw symmetry $\mathcal{S}_{6z}$ can protect the twofold degeneracy at the $q_z = \pi$ plane, which includes the GP1-A path. Since GP2 is a general point offset boundary plane, four separate phonon branches can be captured along the path A-GP2. Figure 3(e) illustrates the 3D phonon dispersion on the q_y-q_z plane. Clearly, along the L-A path ($q_z = \pi$ line), the phonon branches exhibit a twofold degeneracy.

Simultaneously, we employed the PSO method to get the fitting parameters of the four-band model for QDPs at A. Figures 3(c) and 3(f) present our results, where the $k \cdot p$ model (red points) agreed well with the DFT calculations (dark-gray lines). P1 and P2 are two general points in the $q_z = \pi$ plane, with the gray lines representing twofold degenerate phonon branches. This demonstrates that this model is capable of producing twofold phonon degeneracy within the plane. Since P3 and P4 are two general points out of the $q_z = \pi$ plane, the $k \cdot p$ model can also produce four well-separated phonon branches around A. We utilized our model to fit not only the QDP at 3.396 THz but also the remaining five QDPs. All parameters are summarized in Table I of Appendix B. The in-plane and off-plane phonon dispersion for these QDPs are shown in Fig. 8 and Fig. 9 of Appendix B. These results exhibit the characteristics of QDP at A.

C. Type-III nodal ring

Next, we will focus on the type-III NRs at the $q_z = 0$ plane. As well known, kagome lattices are an ideal platform for hosting flat bands, as shown in Figs. 1(b) and 1(c). From the perspective of the tight-binding model, the unit cell has three atoms, and the nearest-neighbor (NN) hopping with t can produce a flat band with an energy level of $2t$. However, in the case of $BaNa_2$, the kagome lattice would be distorted if the next-nearest-neighbor (NNN) atoms are taken into account, as depicted in Fig. 2(a). The Na1 atom is located above one of the centers of the triangular lattice formed by Na2 atoms. Two different triangular lattices are shown in Figs. 1(b) and 7 of Appendix A. The position of the flat band can be tuned from the bottom to the top of the three bands by changing the hopping parameters [24]. Therefore, with varying local force constants in different triangular lattices, a flat nodal ring can be expected for the $BaNa_2$ system.

Here, we demonstrated the existence of a flat nodal ring around 3.93 THz at the $q_z = 0$ plane in $BaNa_2$. As shown in Fig. 2(c), there are two band crossings along the Γ-K and Γ-M paths. These degenerate points are not isolated but rather lie on a ring centered at Γ. As proof, we investigated the band crossings on the $q_z = 0$ plane using a series of paths from Γ-M to Γ-K [blue solid lines in Fig. 2(b)]. In Fig. 4(a), the nodal ring is evidenced by the existence of phonon crossings on all paths (Γ-M, Γ-Q, Γ-P, and Γ-K). All four crossings arise at nearly the same energy level. The energy variations for the lower branch of each path are less than 0.03 THz, suggesting a flat band on the $q_z = 0$ plane. To identify the type-III NR, we present the 3D phonon dispersion in Fig. 4(b). One of the two bands exhibits a flat energy band that is responsible for generating the type-III nodal ring. The energy difference between the two bands is also shown at the bottom of Fig. 4(b). Specifically, one can observe that all the gapless crossings form a closed ring (the brightness part), centered at the Γ point on the $q_z = 0$ plane, at approximately 3.93 THz.

For a NR system, we calculated the Berry phase to confirm their topological properties. The Berry phase is defined as $\gamma_n = \oint_C \mathbf{A}_n(\mathbf{q}) \cdot d\mathbf{q}$, where $\mathbf{A}_n(\mathbf{q}) = -i\langle u_n(\mathbf{q})|\nabla_q|u_n(\mathbf{q})\rangle$ is the Berry connection and $u_n(\mathbf{q})$ is the Blöch wavefunction of the n-th band. As Fig. 4(c) shows, for points on the high-symmetry line K-Γ-M, we calculated the Berry phase by a closed path along the q_z direction (also known as the Zak phase). The Berry phase equals 0 within the NR, but π outside the NR. Therefore, the nontrivial topological surface states can be observed outside the NR, as depicted in Fig. 6(b). There are two independent symmetries that protect the flat NR. The $\mathcal{PT}$ symmetry enforces the Berry phase to have a quantized number of π, preventing the nodal ring to be gapped with respect to perturbations, as long as the $\mathcal{PT}$ symmetry is present. In addition, the mirror symmetry, $\tilde{M}_z = \{M_z|00\frac{1}{2}\}$, will protect the two branches with opposite $\tilde{M}_z$ eigenvalues, resulting in a flat NR lying on the $q_z = 0$ plane.

We utilized a two-band $k \cdot p$ effective model to confirm the presence of a type-III nodal ring around the Γ point within the $q_z = 0$ plane. The general two-band Hamiltonian for phonons, described by

$$\mathcal{H}_{\text{eff}}(\mathbf{q}) = \sum_{i=0}^{3} h_i(\mathbf{q})\sigma_i, \tag{5}$$

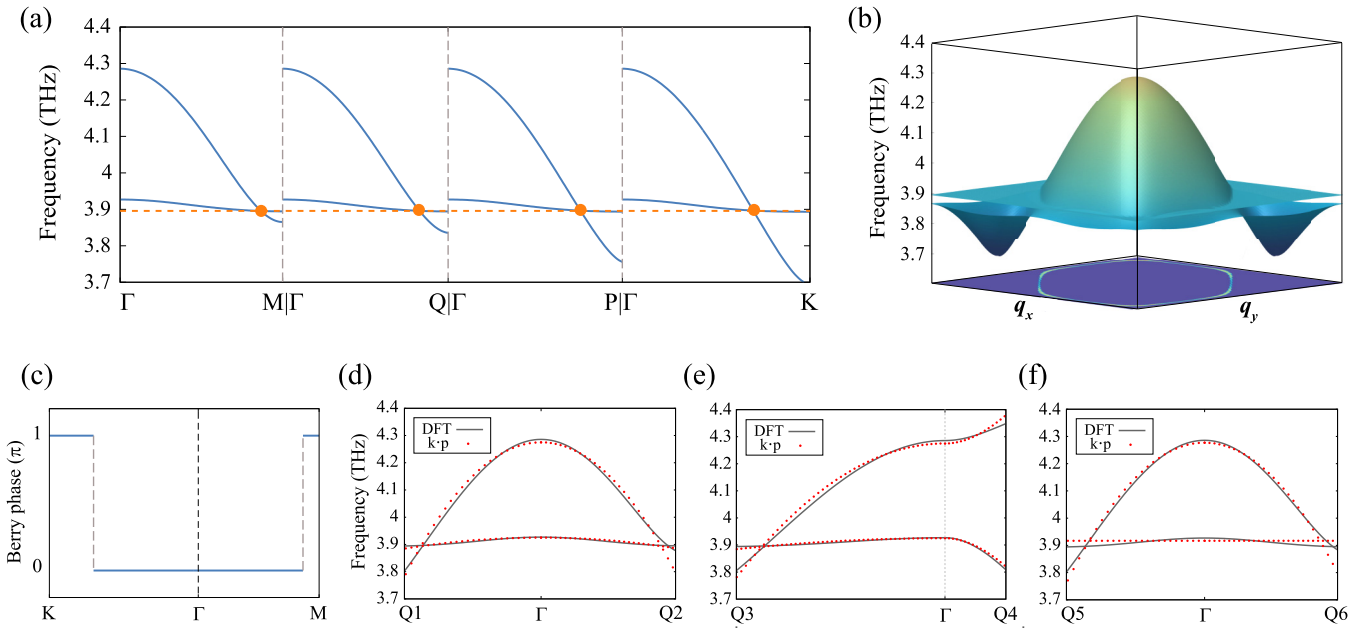

FIG. 4. (a) Phonon dispersions along the Γ-M (Q, P, K) paths. (b) 3D representation of phonon bands correspond to the flat band within the $q_z = 0$ plane and the 2D projection of the phononic nodal ring within the same plane. (c) Variation of Berry phase along the K-Γ-M path within the $q_z = 0$ plane. (d)–(f) Comparison between DFT and $k \cdot p$ model of the type-III nodal ring along different paths, Q1–Q6 are the general points on each path. The dark-gray lines correspond to DFT calculations, while the red dots represent the $k \cdot p$ results. (d) Phonon dispersion along the high-symmetry path K-Γ-M. (e) Phonon dispersion along a general path that passes through the Γ point. (f) Phonon dispersion along the high-symmetry path K-Γ-M when $t_1 = t_5$.

involves real functions $h_i(\mathbf{q})$ (i=0, 1, 2, 3), where $\mathbf{q} = (q_x, q_y, q_z)$ represents the wave vector centered at Γ. Symmetry analysis reveals that the 1D IRs for two branches of flat nodal rings belong to A_{2u} and A_{1g} of the abstract group G_{24}^5. $BaNa_2$ crystallizes in the SG $P6_3/mmc$, with symmetry at the Γ point characterized by the D_{6h} point group, including the inversion symmetry $\mathcal{P}$ and the mirror symmetry $\tilde{M}_z$. Additionally, the phonon system maintains the time-reversal symmetry $\mathcal{T}$. For points within the $q_z = 0$ plane, these three operators commute with each other (see details in Appendix C). We chose the eigenstates of inversion symmetry as basis functions, which is represented by σ_3, indicating two crossing bands with opposite parities.

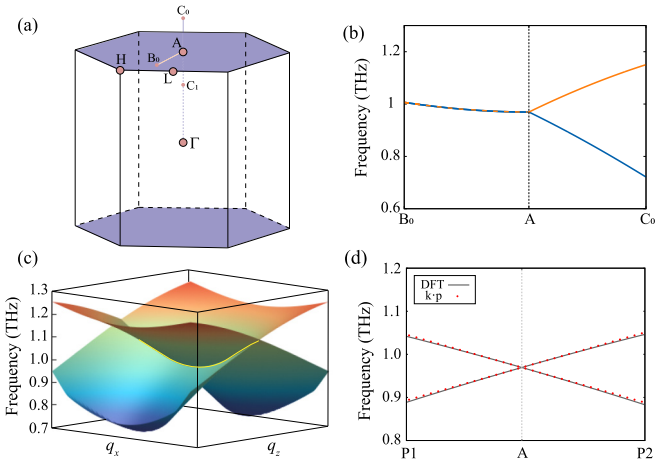

FIG. 5. (a) Schematic diagram of nodal surface states present in the $q_z = \pi$ plane. (b) Phonon dispersions along the B_0-A-C_0 path. Note that B_0 is a general point within the $q_z = \pi$ plane, and C_0 is a general point out of the $q_z = \pi$ plane. (c) 3D phononic bands within the q_x-q_z plane. (d) Comparison between DFT bands with the $k \cdot p$ model bands for the nodal surface along P1-A-P2. P1 and P2 are two general points at the C_0-A and A-C_1, respectively. Dark-gray lines represent DFT calculations, and red dots represent the $k \cdot p$ results. All points in panels (b) and (d) are labeled in panel (a).

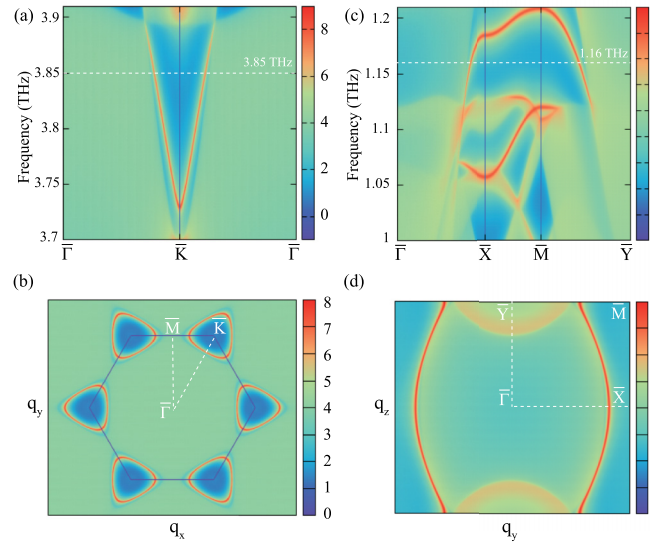

FIG. 6. Phonon surface states of $BaNa_2$. (a) Phonon LDOS projected on the (0001) surface. (c) Phonon LDOS projected on the $(10\bar{1}0)$ surface. The constant energy slices in panels (b) and (d) correspond to the white dashed lines depicted in panels (a) and (c), respectively.

In the absence of spin-orbit coupling (SOC), $\mathcal{T}^2 = 1$, and $\mathcal{T}$ is represented by the matrix $\sigma_0\mathcal{K}$. Combining $\mathcal{P}$ and $\mathcal{T}$ symmetries, the four real functions in effective Hamiltonian Eq. (5) must satisfy the following constraints:

$$h_1(\mathbf{q}) = 0, \quad h_2(\mathbf{q}) = -h_2(-\mathbf{q}), \quad h_{0,3}(\mathbf{q}) = h_{0,3}(-\mathbf{q}). \quad (6)$$

The eigenvalues of $\mathcal{H}_{\text{eff}}(\mathbf{q})$ are expressed as $E_{\pm}(\mathbf{q}) = h_0(\mathbf{q}) \pm \sqrt{h_2^2(\mathbf{q}) + h_3^2(\mathbf{q})}$. After expanding the effective Hamiltonian to the second order, we determined the location of nodal rings by the intersection line of two surfaces represented by $h_{2,3}(\mathbf{q}) = 0$ (see Appendix C). However, the nodal ring centered at Γ requires an additional mirror symmetry $\tilde{M}_z$ to stay on the $q_z = 0$ plane. The matrix representation of the operator $\tilde{M}_z$ is σ_3, since it commutes with the operator $\mathcal{I}$ (see Appendix C). By applying $\tilde{M}_z$ to the system, we obtained the effective Hamiltonian to the third order:

$$\mathcal{H}_{\text{eff}}(\mathbf{q}) = (E_0 + t_1 q_+ q_-)\mathbb{I}_2 + \left(t_2 q_z + t_3 q_z^3\right)\sigma_2 + (t_4 + t_5 q_+ q_-)\sigma_3, \quad (7)$$

where E_0 and t_i (i ∈[1, 5]) are real parameters. The Hamiltonian $\mathcal{H}_{\text{eff}}(\mathbf{q})$ guarantees a nodal ring on the $q_z = 0$ plane. Specifically, the $\tilde{M}_z$ symmetry plays a crucial role in constraining the nodal ring to the $q_z = 0$ plane, by satisfying specific constraints on $h_2(\mathbf{q})$ [see Eq. (C8) of Appendix C]. By analyzing the eigenvalues of the effective Hamiltonian, an exact flat band emerged at $t_1/t_5 = 1$. Fitting the effective Hamiltonian to DFT calculations for the flat nodal ring in $BaNa_2$, the following is obtained: $E_0 = 4.100$ THz, $t_1 = -1.180$ THz Å^2, $t_2 = -1.500$ THz Å, $t_3 = -6.000$ THz Å^3, $t_4 = 0.175$ THz, and $t_5 = -1.095$ THz Å^2.

Figure 4 presents a comparison between the band structures predicted by the $k \cdot p$ model and those obtained from DFT calculations. Q1 and Q2 are points located on the high-symmetry lines K-Γ and M-Γ, respectively. A general point on the $q_z = 0$ plane, located outside the nodal ring, is denoted by Q3 (0.23, 0.31, 0.0), while Q4 (0.0, 0.0, 0.27) indicates a general point on the high-symmetry line Γ-A. Evidently, in Figs. 4(d) and 4(e), the model reproduces the phonon dispersions accurately both in-plane and out-of-plane throughout a broad range of reciprocal space. The third-order term in Eq. (7) yields the nonlinear out-of-plane dispersion (further details are provided in Appendix C). Due to the small dispersion of the nodal ring on the plane, t_1/t_5 is nearly equal to 1. This effective Hamiltonian is capable of producing a perfectly flat band under the critical condition of $t_1 = t_5$, as shown in Fig. 4(f). Notably, the ratio of t_1/t_5, which corresponds to the kinetic and potential energy ratios, can be manipulated to control the flatness of the band.

D. Nodal surface

Here, we turn to investigate the NSs on the $q_z = \pi$ plane. The NS indicates that all points on the plane are twofold degenerate, as shown in Fig. 1(d). For $BaNa_2$, degenerate phonon bands exist along the high-symmetry line A-H-L-A on the $q_z = \pi$ plane [see all the branches highlighted in orange color in Fig. 2(c)]. In addition to the high-symmetry line, the twofold degenerate band can also be observed along the B_0-A path of the plane $q_z = \pi$ [Fig. 5(b)]. However, on the A-C_0 out-of-plane path, the twofold degenerate bands split into two single branches. Figure 5(c) displays the 3D phonon dispersion of the wave vectors on the q_x-q_z plane. The two phonon branches cross at the condition of $q_z = \pi$, forming a twofold degenerate band [see the yellow line in Fig. 5(c)]. This degeneracy supports that all phonon branches on the $q_z = \pi$ plane are twofold degenerate, resulting in a nodal surface on this plane.

Our symmetry analysis demonstrated that the combination of a twofold screw symmetry $\mathcal{S}_{2z}$ and $\mathcal{T}$ symmetry gives rise to the nodal surface in SG $P6_3/mmc$. The $\mathcal{S}_{2z}$ can be generated by combining mirror reflection $\tilde{M}_z$ and inversion symmetry $\mathcal{P}$. Furthermore, the nonsymmorphic symmetry $\mathcal{S}_{2z} = \{C_2|00\frac{1}{2}\}$ produces a half-translation along the rotation axis that reverses q_x and q_y in reciprocal space. Since the spinless phonon system satisfies $\mathcal{T}^2 = 1$, the $\mathcal{T}\mathcal{S}_{2z}$ operator preserves $\mathbf{q}$ on the $q_z = \pi$ plane at the BZ boundary, giving the following relationship:

$$(\mathcal{T}\mathcal{S}_{2z})^2 = e^{-iq_z}. \quad (8)$$

Applying $\mathcal{T}\mathcal{S}_{2z}$ twice results in a translation along the z direction by a lattice constant. On the $q_z = \pi$ plane, similar to Kramers' degeneracy, $(\mathcal{T}\mathcal{S}_{2z})^2 = -1$ indicates that all phonon branches on this plane should be degenerate, constrained by the antiunitary symmetry $\mathcal{T}\mathcal{S}_{2z}$. The two degenerate phonon branches can be labeled by eigenvalues ±i of $\mathcal{T}\mathcal{S}_{2z}$, and two related states of Kramers' pair will have the same eigenvalues for $\mathcal{H}_{\text{eff}}(\mathbf{q})$. If this antiunitary symmetry were broken, the twofold degenerate state would vanish along the A-C_0 out-of-plane path [Fig. 5(b)]. Therefore, the nodal surface is only protected on the $q_z = \pi$ plane. Similar to the type-III NRs, we found that the NS in $BaNa_2$ exhibits a narrow phonon dispersion. The dispersionless band is expected to produce a large phononic DOS, which would, in turn, facilitate experimental observations.

We derived a two-band $k \cdot p$ model to clarify the topological feature of the nodal surface. We obtained that $h_{0,3}$ should be even functions whereas h_2 should be odd function, as they share the same $\mathcal{P}\mathcal{T}$ symmetry [see Eq. (6)]. In addition to the $\mathcal{P}\mathcal{T}$ constraints, we must also consider two other symmetries, mirror reflection $\tilde{M}_z$, and rotation symmetry C_{2xy}. As $[C_{2xy}, \mathcal{I}] = 0$ and $\{\tilde{M}_z, \mathcal{I}\} = 0$ (see detailed derivations in Appendix D), we chose $C_{2xy} = \sigma_3$ and $\tilde{M}_z = \sigma_1$. Applying the two symmetry operations to the effective Hamiltonian yielded:

$$\mathcal{H}_{\text{eff}}(\mathbf{q}) = E_0\sigma_0 + t_1 q_z \sigma_2, \quad (9)$$

where E_0 and t_1 are real parameters. By fitting the DFT calculated fifth and sixth phonon branches (Fig. 2), we obtained $E_0 = 0.969$ THz and $t_1 = 2.380$ THzÅ. Again, a good agreement was achieved between model predictions and DFT calculations [see Fig. 5(d)]. In particular, the model accurately reproduced the linear dispersion of the bands that are not in the $q_z = \pi$ plane and exhibited exact twofold degeneracy for the bands on that plane. Additionally, the same model has been used to describe other nodal surfaces (see Appendix D).

E. Nontrivial surface states

As the nodal ring and nodal surface are characterized by the existence of topological surface states, here we calculated the surface states of (0001) and (10$\bar{1}$0) surfaces. Figure 6 shows the calculated local density of states (LDOS) of phonons. As illustrated in Fig. 6(a), nontrivial drumhead surface states induced by topological nodal ring can be observed around the high-symmetry points $\bar{K}$ along the $\bar{\Gamma}$-$\bar{K}$-$\bar{\Gamma}$ path. This was in good agreement with our calculated Berry phase distributions [Fig. 4(c)]. These nontrivial surface states originates from the crossing points of the NR around 3.9 THz and have a large dispersion up to 3.72 THz, which was beneficial to the experimental observation. Figure 6(b) presents the isofrequency surface states for the (0001) surface. The LDOS on this isofrequency surface shows a good agreement with the phonon surface states shown in Fig. 6(a). As anticipated, the surface phonon arcs display hexagonal symmetry in the surface BZ, arising from the sixfold rotation symmetry of $BaNa_2$.

The NSs are located on the $q_z = \pi$ plane, so observing the nontrivial surface states on the (0001) surface is challenging, as these overlap with bulk states. Therefore, we presented the LDOS on the (10$\bar{1}$0) surface BZ. Considering the frequency range of dispersion, we focused on the nodal surface around 1.2 THz. The nodal surface was projected onto both the upper and lower boundaries of the BZ. As shown in Fig. 6(c), the nontrivial surface states with high LDOS are clearly visible around $\bar{X}$ and $\bar{M}$. The isofrequency surface states of the (10$\bar{1}$0) surface was also calculated and depicted in Fig. 6(d). Clearly, the surface states go through the whole BZ and connect the $q_z = \pm\pi$ plane.

Identifying the surface states associated with DPs is also difficult due to the overlap with bulk states (see Fig. 13 in Appendix E). Although the nontrivial surface states of $BaNa_2$ presented above are limited to specific phonon frequencies, they should be observable for a wide range of frequencies due to the wide distribution of symmetry-enforced topological phonons.

IV. CONCLUSION

In summary, through the combination of symmetry analysis, $k \cdot p$ model, and first-principles calculations, we have demonstrated that $BaNa_2$ of the C14 Laves phase AB2 is an ideal material for realizing the coexistence of QDPs, type-III NRs, and NSs. This property is a consequence of the symmetry protection provided by the space group $P6_3/mmc$. The existence of QDPs, which are protected by the nonsymmorphic symmetry $\mathcal{S}_{6z}$ and C''_{21}, as well as the $\mathcal{PT}$ symmetry, is guaranteed by the 4D IR of A_3^4. The type-III NRs associated with flat bands are protected by the $\mathcal{PT}$ symmetry, and the presence of mirror symmetry guarantees their location on the reflection-invariant plane. The ideal NS, characterized by twofold degenerate phonon bands, exists in the $q_z = \pi$ plane, and its presence is protected by both screw rotation and time-reversal symmetries. Based on the symmetry analysis, we derived effective $k \cdot p$ models, which can accurately describe all the QDPs, type-III NRs, and NSs of $BaNa_2$ across a wide range of the BZ. We verified the nontrivial nature of the nodal ring and nodal surface by identifying topological surface states through the LDOS calculations. Considering that $BaNa_2$ single crystals can be experimentally synthesized [94], exhibit stability under ambient conditions, and possess weak metallic bonding that facilitates the exfoliation of atomically sharp surfaces, we anticipate that our findings regarding $BaNa_2$ will inspire experimental investigations and detections. Finally, based on our established topological phonon database [25,26], we screened out nine additional materials that can also host QDPs, type-III NRs, and NSs simultaneously. The phonon dispersion relationships of these materials are given in Fig. 14 of Appendix F. Our work showcases the important role of crystal symmetry in the exploration of materials exhibiting fascinating topological phonons, and paves the way for investigating topological phononic materials that possess hybrid topological features.

TABLE II. $k \cdot p$ model parameters for NSs.

Phonon branches	t_0 (THz)	t_1 (THzÅ)	Phonon branches	t_0 (THz)	t_1 (THzÅ)
1–2	0.572	2.000	3–4	0.572	2.020
5–6	0.969	2.380	7–8	1.618	0.880
9–10	1.707	0.800	11–12	1.707	0.810
13–14	2.028	0.018	15–16	2.028	0.020
17–18	2.392	0.036	19–20	2.439	1.000
21–22	2.625	1.140	23–24	2.625	1.142
25–26	3.168	0.860	27–28	3.168	0.858
29–30	3.395	0.022	31–32	3.395	0.023
33–34	3.567	2.100	35–36	4.437	0.600

ACKNOWLEDGMENTS

This work is supported by the National Key R&D Program of China (Grant No. 2021YFB3501503), National Natural Science Foundation of China (Grant No. 51474202), Network and Information Foundation of CAS (Grant No. CAS-WX2021SF-0102), and the Key project of Chinese Academy of Sciences (Grant No. ZDRW-CN-2021-2-5). J.X. Li also acknowledges the funding from China Postdoctoral Science Foundation (Grants No. 2022T150660 and No. 2021M700152).

APPENDIX A: CRYSTAL STRUCTURE OF $BaNa_2$

Figure 7 displays thedetailed crystal structure of $BaNa_2$. Na1 atoms are arranged in 2D triangular lattices, whereas Na2 atoms are in kagome lattices, as shown in Figs. 7(a) and 7(b). All Na atoms form the hexahedron illustrated in Fig. 7(c). The eigenvectors of the dynamical matrix provide the vibrational modes of the flat band. Na1 and Na2 atoms vibrate in opposite directions along the z axis, which disturbs the local force constants of a perfect kagome lattice. As a result, the intrinsic flat band position in the kagome lattice changes, producing a critical condition where a flat nodal ring (type-III nodal ring) can be anticipated.

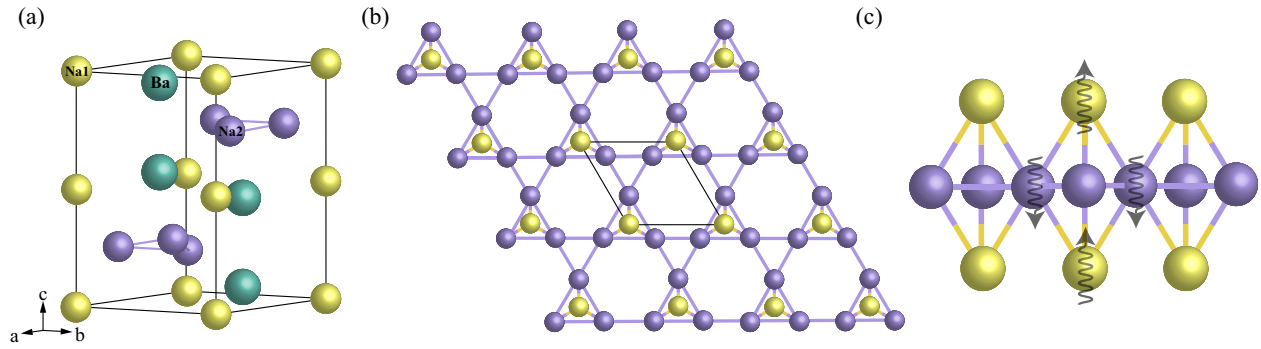

FIG. 7. (a) Crystal structure of $BaNa_2$. (b) Kagome lattice formed by Na2 atoms, which are affected by Na1 atoms arranged in a triangular lattice. (c) Hexahedron of Na atoms where two layers of Na atoms vibrate in opposite directions.

APPENDIX B: $k \cdot p$ MODEL FOR QUADRATIC DIRAC POINT

In this Appendix, we present the detailed symmetry analysis and derivation of low-energy effective models for SG $P6_3/mmc$ (No.194). As discussed in the main text, the fourfold degenerate crossings at high-symmetry point A (0, 0, 0.5) are QDPs with quadratic dispersion. The little group at A contains three generating elements: a sixfold screw rotation $\mathcal{S}_{6z} = \{C_6^+|00\frac{1}{2}\}$, a twofold rotation $C_{21}'' = \{C_2^+|000\}$, and inversion symmetry $\mathcal{P} = \{\mathcal{I}|000\}$. The system also contains time-reversal symmetry $\mathcal{T}$. Based on the relations of abstract group G_{48}^1, the symmetry operations satisfy the following algebraic relations at A:

$$(\mathcal{S}_{6z})^{12} = (C_{21}'')^2 = \mathcal{I}^2 = E, \tag{B1}$$

$$(\mathcal{S}_{6z})^{11} C_{21}'' = C_{21}'' \mathcal{S}_{6z}, \tag{B2}$$

$$(\mathcal{S}_{6z})^{7} \mathcal{I} = \mathcal{I} \mathcal{S}_{6z}, \tag{B3}$$

$$\mathcal{S}_{6z}\mathcal{T} = \mathcal{T}\mathcal{S}_{6z}, \tag{B4}$$

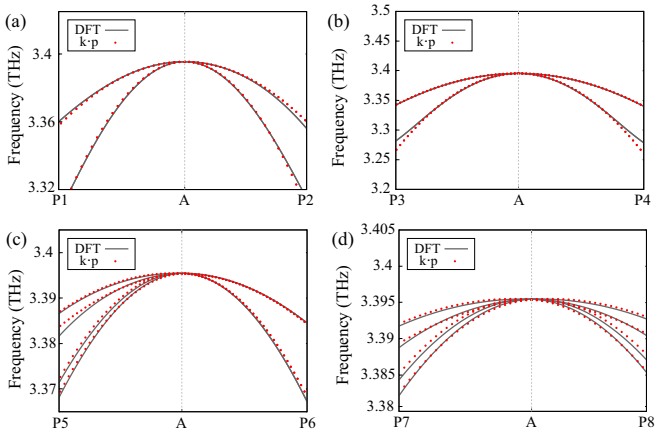

FIG. 8. Comparison between DFT bands and the results from the $k \cdot p$ model around the QDP along different paths, P1-P8 are the general points on each path. Dark-gray lines come from DFT calculations, and red dots come from the $k \cdot p$ model. Phonon dispersion along (a) the high-symmetry path and off (b) the high-symmetry path in $q_z = \pi$ plane. (c, d) Phonon bands along general paths out of the $q_z = \pi$ plane.

where E is the unit operator. Using these equations, we can derive the commutation and anticommutation relations of the symmetry operations.

Here, the sixfold screw symmetry $\mathcal{S}_{6z}$ is along the z axis with a fractional translation vector. Consequently, applying the operation six times yields $\mathcal{S}_{6z}^6 = \{E|3c\}$, which induces a phase factor in the Bloch wavefunction $\varphi_{\mathbf{q}}(\mathbf{r})$ as

$$\mathcal{S}_{6z}^6 \varphi_{\mathbf{q}}(\mathbf{r}) = \{E|3c\}\varphi_{\mathbf{q}}(\mathbf{r}) = e^{-iq_z \cdot 3c}\varphi_{\mathbf{q}}(\mathbf{r}),$$

which indicates $e^{-iq_z \cdot 3c}$ is the eigenvalue of $\mathcal{S}_{6z}^6$. For the sixfold rotation symmetry C_6^+, its eigenvalues are expressed as $e^{i2\pi n/6}$ $(n = 0, 1, \ldots, 5)$. Therefore, the eigenvalues of $\mathcal{S}_{6z}$ can be expressed as $e^{i2\pi n/6} e^{-iq_z \cdot c/2}$ $(n = 0, 1, \ldots, 5)$. We selected four linearly independent eigenstates of $\mathcal{S}_{6z}$ as basis functions (denoted as $|c_{6z}\rangle$) for the point A (0, 0, 0.5). The representation of $\mathcal{S}_{6z}$ is expressed by

$$\mathcal{S}_{6z} = \begin{bmatrix} e^{i\frac{\pi}{6}} & 0 & 0 & 0 \\ 0 & e^{-i\frac{5\pi}{6}} & 0 & 0 \\ 0 & 0 & e^{-i\frac{\pi}{6}} & 0 \\ 0 & 0 & 0 & e^{i\frac{5\pi}{6}} \end{bmatrix}.$$

By utilizing Eqs. (B2) and (B3), we derived

$$(\mathcal{S}_{6z})^{-1} C_{21}'' = C_{21}'' \mathcal{S}_{6z}, \tag{B5}$$

$$\mathcal{I}\mathcal{S}_{6z} = -\mathcal{S}_{6z}\mathcal{I}. \tag{B6}$$

The formula of the time-reversal symmetry $\mathcal{T}$ under the screw rotational representation $\mathcal{S}_{6z}$ was obtained from Eq. (B4):

$$\begin{aligned} \mathcal{S}_{6z}\mathcal{T}|e^{i\frac{\pi}{6}}\rangle &= \mathcal{T}\mathcal{S}_{6z}|e^{i\frac{\pi}{6}}\rangle, \\ \mathcal{S}_{6z}\mathcal{T}|e^{i\frac{\pi}{6}}\rangle &= e^{i\frac{\pi}{6}}\mathcal{T}|e^{-i\frac{\pi}{6}}\rangle. \end{aligned} \tag{B7}$$

For the twofold rotation symmetry C_{21}'', we can obtain the following relations from Eq. (B5):

$$\begin{aligned} (\mathcal{S}_{6z})^{-1} C_{21}''|e^{i\frac{\pi}{6}}\rangle &= C_{21}''\mathcal{S}_{6z}|e^{i\frac{\pi}{6}}\rangle, \\ \mathcal{S}_{6z}C_{21}''|e^{i\frac{\pi}{6}}\rangle &= e^{-i\frac{\pi}{6}}C_{21}''|e^{i\frac{\pi}{6}}\rangle. \end{aligned} \tag{B8}$$

Additionally, Eq. (B6) enables us to derive the inversion symmetry $\mathcal{P}$ by applying it to the eigenstates $|c_{6z}\rangle$:

$$\begin{aligned} \mathcal{S}_{6z}\mathcal{I}|e^{i\frac{\pi}{6}}\rangle &= -\mathcal{I}\mathcal{S}_{6z}|e^{i\frac{\pi}{6}}\rangle, \\ \mathcal{S}_{6z}\mathcal{I}|e^{i\frac{\pi}{6}}\rangle &= e^{-i\frac{5\pi}{6}}\mathcal{I}|e^{i\frac{\pi}{6}}\rangle. \end{aligned} \tag{B9}$$

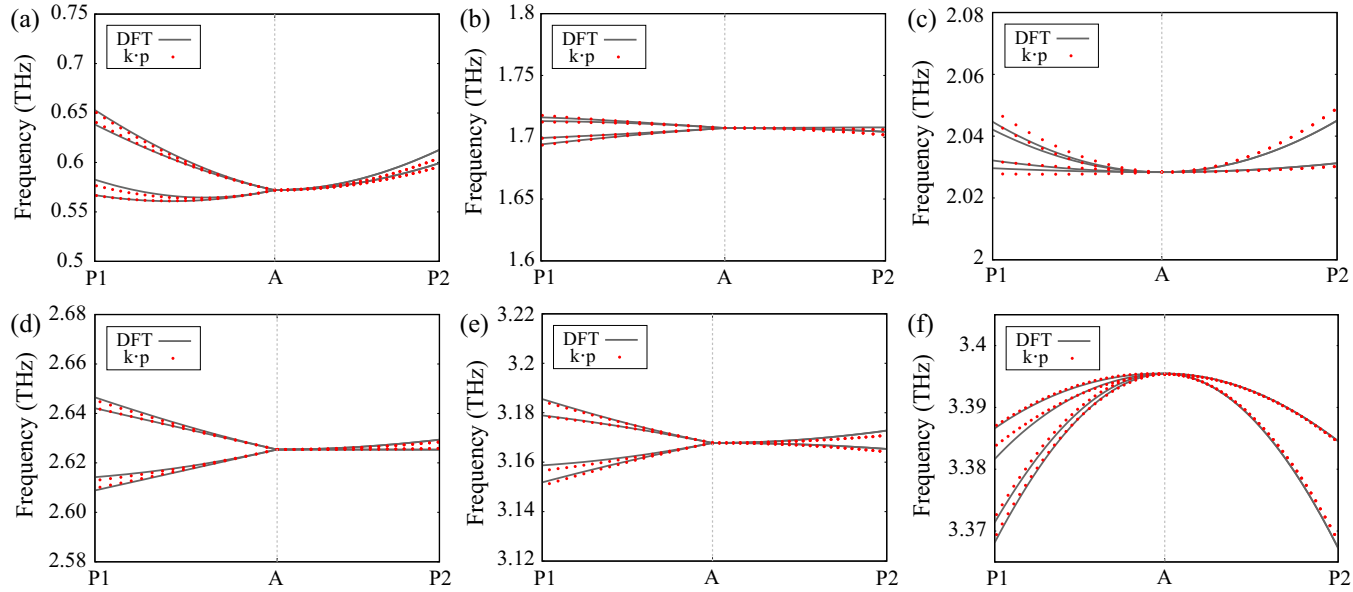

FIG. 9. Comparison between DFT and $k \cdot p$ bands of the QDP along different paths, P1 and P2 are the general points on each path. Dark-gray lines represent the DFT calculation results, and red dots represent the $k \cdot p$ model results. (a–f) Phonon dispersion for QDP along various paths.

By applying the three operators on $|e^{i\frac{5\pi}{6}}\rangle$, we also got similar results. Combining results of Eqs. (B7)–(B9), we obtained the following relationships:

$$\mathcal{T}|e^{i\frac{\pi}{6}}\rangle = |e^{-i\frac{\pi}{6}}\rangle, \mathcal{T}|e^{i\frac{5\pi}{6}}\rangle = |e^{-i\frac{5\pi}{6}}\rangle,$$
$$C_{21}''|e^{i\frac{\pi}{6}}\rangle = |e^{-i\frac{\pi}{6}}\rangle, C_{21}''|e^{i\frac{5\pi}{6}}\rangle = |e^{-i\frac{5\pi}{6}}\rangle,$$
$$\mathcal{I}|e^{i\frac{\pi}{6}}\rangle = |e^{-i\frac{5\pi}{6}}\rangle, \mathcal{I}|e^{-i\frac{\pi}{6}}\rangle = |e^{i\frac{5\pi}{6}}\rangle.$$

Therefore, we can get the matrix representation of the generators as $C_{21}'' = \sigma_1 \otimes \sigma_0$, $\mathcal{I} = \sigma_0 \otimes \sigma_1$, and $\mathcal{T} = \sigma_1 \otimes \sigma_0 \mathcal{K}$, where σ_i $(i = 1, 2, 3)$ are three Pauli matrices, and σ_0 is the 2×2 identity matrix. Using these four operators, we constructed the effective $k \cdot p$ model for the QDP at point A. The Hamiltonian $\mathcal{H}_{\text{eff}}(\mathbf{q})$ is required to be invariant under these symmetry transformations $\hat{O}$,

$$\hat{O}\mathcal{H}_{\text{eff}}(\mathbf{q})\hat{O}^{-1} = \mathcal{H}_{\text{eff}}(\mathcal{R}\mathbf{q}), \tag{B10}$$

where $\mathbf{q}$ is measured from the QDP, $\mathcal{R}$ is the corresponding matrix representation. With the constraint in Eq. (B10), we expressed the effective model up to second-order expansion as

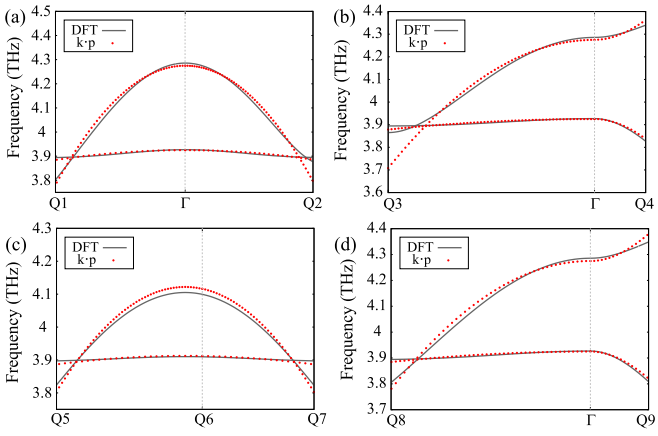

FIG. 10. The comparison between the DFT and $k \cdot p$ bands ($t_1 \neq t_5$) of the type-III nodal ring along different paths, Q1–Q9 are the general points on each path. The DFT bands are depicted as dark-gray lines, while $k \cdot p$ bands are denoted by red dots. (a) Phonon dispersion along the high-symmetry path K-Γ-M. (b) Phonon dispersion along the high-symmetry path M-Γ-A. (c) Phonon dispersion along a general path intersects with the type-III nodal ring off the Γ point. (d) Phonon dispersion along a general path passing through the Γ point.

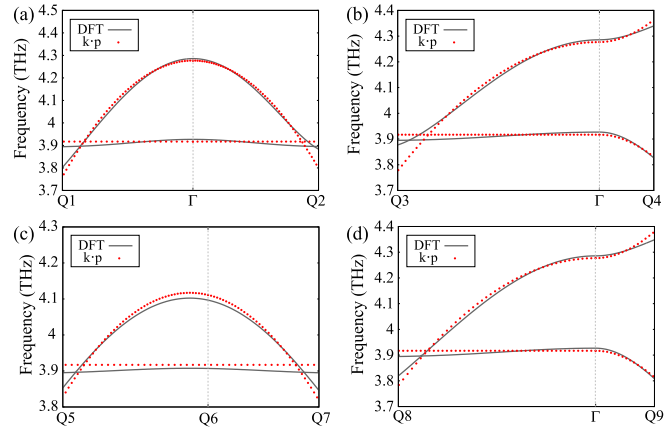

FIG. 11. Comparison of DFT calculation and $k \cdot p$ model results when $t_1 = t_5$ of the type-III nodal ring along different paths, Q1-Q9 are the general points on each path. Dark-gray lines come from DFT calculations, and red dots come from the $k \cdot p$ model. (a) Phonon dispersion along the K-Γ-M path. (b) Phonon dispersion along M-Γ-A path. (c) Phonon dispersion along a general path intersects with the type-III nodal ring off the Γ point. (d) Phonon dispersion along a general path passes through the Γ point.

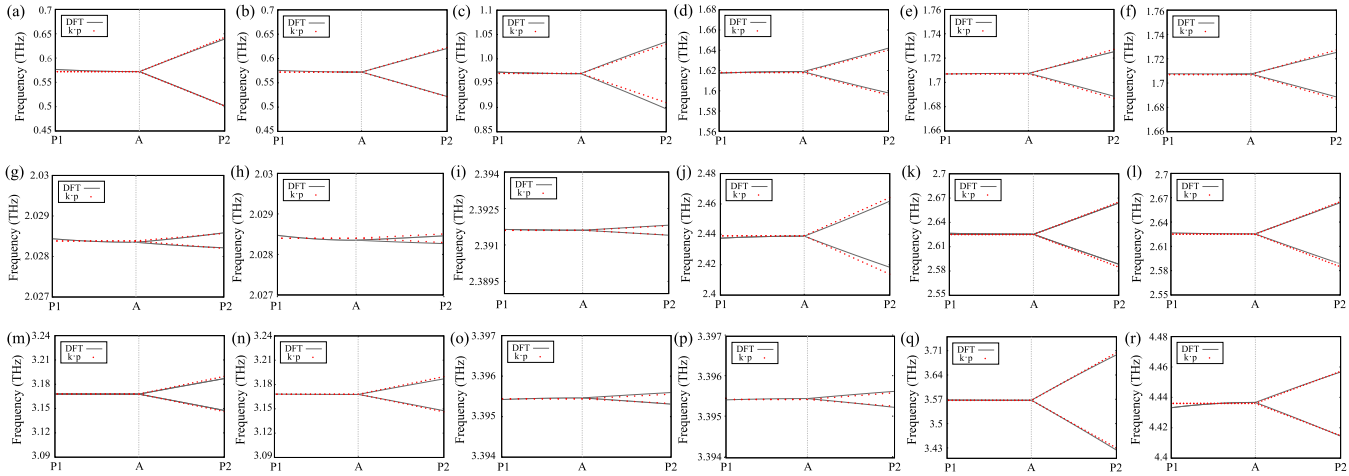

FIG. 12. Comparison between DFT bands and the bands from the $k \cdot p$ model of the nodal surface along different paths, where P1 and P2 are the general points on each path. Dark-gray lines represent the DFT calculations, and red dots represent the $k \cdot p$ model results. (a)–(r) The phonon dispersions for nodal surfaces along different paths.

follows:

$$\mathcal{H}_{\text{eff}}(\mathbf{q}) = \begin{bmatrix} E_0 + t_1 q_x^2 + t_1 q_y^2 + t_2 q_z^2 + t_3 q_z & 0 & t_4 q_x q_z(-1-i) + t_4 q_y q_z(1-i) & i t_5 q_x^2 + 2 t_5 q_x q_y - i t_5 q_y^2 \\ 0 & E_0 + t_1 q_x^2 + t_1 q_y^2 + t_2 q_z^2 - t_3 q_z & i t_5 q_x^2 + 2 t_5 q_x q_y - i t_5 q_y^2 & t_4 q_x q_z(-1-i) + t_4 q_y q_z(1-i) \\ t_4 q_x q_z(-1+i) + t_4 q_y q_z(1+i) & -i t_5 q_x^2 + 2 t_5 q_x q_y + i t_5 q_y^2 & E_0 + t_1 q_x^2 + t_1 q_y^2 + t_2 q_z^2 - t_3 q_z & 0 \\ -i t_5 q_x^2 + 2 t_5 q_x q_y + i t_5 q_y^2 & t_4 q_x q_z(-1+i) + t_4 q_y q_z(1+i) & 0 & E_0 + t_1 q_x^2 + t_1 q_y^2 + t_2 q_z^2 + t_3 q_z \end{bmatrix}, \tag{B11}$$

where $q_{x,y,z}$ are momentum offset relative to point A, E_0 is the frequency of fitted branches at point A, and t_n (n $\in [1, 5]$) are real coefficients. The symmetry-allowed effective Hamiltonian $\mathcal{H}_{\text{eff}}(\mathbf{q})$ in Eq. (B11) can be used to reproduce the dispersion features of QDP at point A.

We selected the QDP around 3.396 THz as the target point to verify the validity of our model. The eigenvalues of 1000 $\mathbf{q}$ points around point A have been used as input for model fitting by the PSO method. To get the ideal model, we randomly generated these 1000 points within the BZ. The fitted parameters are $E_0 = 3.396$ THz, $t_1 = -1.190\,\text{THzÅ}^2$, $t_2 = 0.040\,\text{THzÅ}^2$, $t_3 = 0.060$ THzÅ, $t_4 = 0.160\,\text{THzÅ}^2$, and $t_5 = 0.500\,\text{THzÅ}^2$.

As shown in Fig. 8, the phonon dispersions around the QDP at point A have been obtained from both DFT calculations (dark-gray lines) and the $k \cdot p$ model (red dots). Clearly, the $k \cdot p$ model after PSO fitting accurately reproduces the phonon dispersions, revealing the symmetry-constrained states both in degeneracy and frequency. To systematically study the QDPs, the $k \cdot p$ model was used to fit the other five QDPs. The fitting parameters for these six QDPs are summarized in Table I. From the fitting results, we observed that t_4 is a constant that is related to the dispersion along the q_z direction. Therefore, we can expect a linear dispersion along the q_z direction, which is also verified in the model for the NS.

To verify the generality of our model, the phonon dispersions for all QDPs at A point are shown in Fig. 9. P1 refers to a general point out of the plane, whereas P2 is a point in the $q_z = \pi$ plane. The paths P1-A and P2-A illustrate the main feature of the QDP: (i) the fourfold degeneracy at A; (ii) the quadratic dispersion around A; (iii) the twofold degeneracy for branches in the $q_z = \pi$ plane. The $k \cdot p$ model accurately reproduces the DFT results for each QDP. Notably, t_1 determines both the quadratic dispersion orientation and magnitude of the dispersion slope.

APPENDIX C: $k \cdot p$ MODEL FOR TYPE-III NODAL RING

In this Appendix, we present details for deriving a two-band $k \cdot p$ effective Hamiltonian to get a deeper understanding of the flat nodal ring (type-III nodal ring). We begin with a general two-band model described by

$$\mathcal{H}_{\text{eff}}(\mathbf{q}) = \sum_{i=0}^{3} h_i(\mathbf{q})\sigma_i = \begin{bmatrix} h_0 + h_3 & h_1 - i h_2 \\ h_1 + i h_2 & h_0 - h_3 \end{bmatrix}, \tag{C1}$$

where $h_i(\mathbf{q})$ ($i \in [0, 3]$) are real functions, and $\mathbf{q} = (q_x, q_y, q_z)$ represents the momentum in the BZ. In this Appendix, we use symmetry operations on the general model to derive an effective two-band Hamiltonian. Based on these symmetry arguments, we found that the abstract group of the Γ point in SG $P6_3/mmc$ belongs to G_{24}^5. Moreover, the D_{6h} point group can provides us with the inversion symmetry $\mathcal{P} = \{\mathcal{I}|000\}$ and mirror symmetry $\tilde{M}_z = \{M_z|00\frac{1}{2}\}$. Additionally, the phonon system obeys time-reversal symmetry $\mathcal{T}$. We begin with two basic symmetries, $\mathcal{P}$ and $\mathcal{T}$, that satisfy $\mathcal{I}^2 = \mathcal{T}^2 = 1$.

Here, we selected σ_3 as the matrix representation of $\mathcal{P}$ symmetry, which corresponds to opposite parities of the two

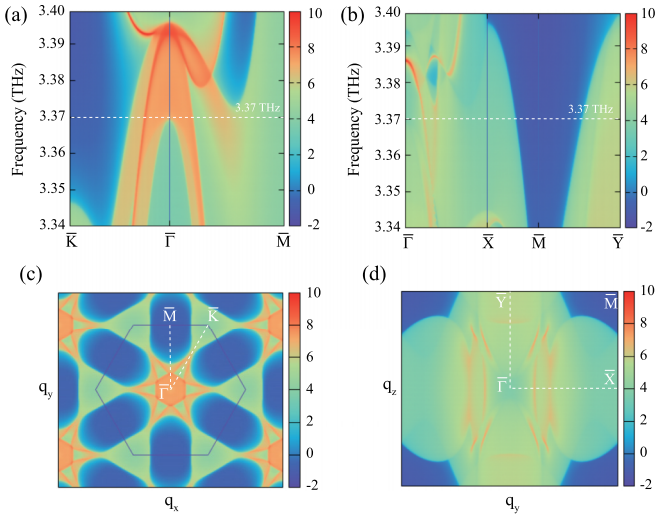

FIG. 13. Phonon surface states of the quadratic Dirac point at around 3.396 THz. (a) Phonon LDOS projected on the (0001) surface. (b) Phonon LDOS projected on the $(10\bar{1}0)$ surface. The isofrequency surface states in panels (c) and (d) correspond to the white dashed lines depicted in panels (a) and (c), respectively.

bands. Due to the commutation relation between $\mathcal{P}$ and $\mathcal{T}$, $[\mathcal{P}, \mathcal{T}] = 0$. The matrix representation of $\mathcal{T}$ operator under the parity representation can be expressed as $\mathcal{T} = \sigma_0 \mathcal{K}$.

Applying these two operators to the model Hamiltonian yields the following results:

$$\mathcal{H}(\mathcal{I}\mathbf{q}) = \mathcal{I}\mathcal{H}(\mathbf{q})\mathcal{I}^{-1}, \tag{C2}$$

$$\mathcal{H}(\mathcal{T}\mathbf{q}) = \mathcal{T}\mathcal{H}(\mathbf{q})\mathcal{T}^{-1}. \tag{C3}$$

Equation (C2) reveals the even and odd properties of real functions h_i given by

$$h_{1,2}(\mathbf{q}) = -h_{1,2}(-\mathbf{q}),$$
$$h_{0,3}(\mathbf{q}) = h_{0,3}(-\mathbf{q}).$$

Similarly, Eq. (C3) verifies the even and odd properties of real functions h_i under $\mathcal{T}$ symmetry given by

$$h_{0,1,3}(\mathbf{q}) = h_{0,1,3}(-\mathbf{q}),$$
$$h_2(\mathbf{q}) = -h_2(-\mathbf{q}).$$

According to the above relations, it is evident that $h_1 = 0$, h_2 is an odd function, and $h_{0,3}$ are even functions of $\mathbf{q}$. Therefore, the symmetry-allowed $h_i(\mathbf{q})$ functions up to second-order terms are represented as

$$h_1(\mathbf{q}) = 0,$$
$$h_2(\mathbf{q}) = \sum_{i=x,y,z} t_i q_i,$$
$$h_{0,3}(\mathbf{q}) = m_0 + \sum_{i=x,y,z} m_i q_i^2, \tag{C4}$$

where t_i $(i = x, y, z)$ are three real parameters, and m_0 and m_i $(i = x, y, z)$ are also real parameters. The phonon dispersions of the two-band Hamiltonian Eq. (C1) around the Γ point are

$$E(\mathbf{q}) = h_0(\mathbf{q}) \pm \sqrt{h_2^2(\mathbf{q}) + h_3^2(\mathbf{q})}.$$

Based on the above analysis, the location of phonon crossings is determined by the conditions $h_2(\mathbf{q}) = 0$ and $h_3(\mathbf{q}) = 0$. Due to the power of expansion, the nodal ring can be expected by the intersection of a plane and a closed surface, both of which are centered at Γ point. It is restricted by additional symmetry to the Γ-M-K plane.

Next, we will consider the nonsymmorphic symmetry $\tilde{M}_z$. In real space, the mirror symmetry $\tilde{M}_z = \{M_z|00\frac{1}{2}\}$ and inversion symmetry $\mathcal{P}$ change the coordinates as

$$\mathcal{I} : (x, y, z) \mapsto (-x, -y, -z),$$
$$\tilde{M}_z : (x, y, z) \mapsto \left(x, y, -z + \tfrac{1}{2}\right). \tag{C5}$$

From the above conditions, we know that

$$\mathcal{I}\tilde{M}_z : (x, y, z) \mapsto \left(-x, -y, z - \tfrac{1}{2}\right), \tag{C6}$$

$$\tilde{M}_z\mathcal{I} : (x, y, z) \mapsto \left(-x, -y, z + \tfrac{1}{2}\right). \tag{C7}$$

This implies that $\mathcal{I}\tilde{M}_z = e^{iq_z \cdot 2\pi}\tilde{M}_z\mathcal{I}$. $\tilde{M}_z$ and $\mathcal{I}$ operators will commute with each other on the $q_z = 0$ plane, $[\mathcal{I}, \tilde{M}_z] = 0$. Under the parity representation, we can express $\tilde{M}_z$ as σ_3 in terms of the irreducible representations ± 1 of $\tilde{M}_z$. Consequently, we obtain

$$\mathcal{H}(\tilde{M}_z\mathbf{q}) = \tilde{M}_z\mathcal{H}(\mathbf{q})\tilde{M}_z^{-1}.$$

The transformation matrix for $\tilde{M}_z$ is represented as

$$\begin{bmatrix} 1 & 0 & 0 \\ 0 & 1 & 0 \\ 0 & 0 & -1 \end{bmatrix}.$$

Substituting $\tilde{M}_z$ with σ_3 yields additional constraints on h_i functions, expressed as follows:

$$h_{0,3}(q_x, q_y, q_z) = h_{0,3}(q_x, q_y, -q_z),$$
$$h_{1,2}(q_x, q_y, q_z) = -h_{1,2}(q_x, q_y, -q_z). \tag{C8}$$

To achieve the target nodal ring on the $q_z = 0$ plane, the coefficients of $q_{x,y}$ items in $h_{1,2}$ should be excluded, and the q_z^2 items in $h_{0,3}$ can also be omitted. Hence, the two-band effective model, expanded up to the third order of $\mathbf{q}$ around the Γ point, was given by

$$\mathcal{H}_{\text{eff}}(\mathbf{q}) = (E_0 + t_1 q_+ q_-)\mathbb{I}_2 + (t_2 q_z + t_3 q_z^3)\sigma_2 + (t_4 + t_5 q_+ q_-)\sigma_3. \tag{C9}$$

When the two bands cross, $h_2(q_z)$ is identically zero on the $q_z = 0$ plane, and consequently, it confines the nodal ring to the q_x-q_y plane centered at the Γ point. From the eigenvalues of this model, we know that t_1 and t_5 coefficients would determine whether the nodal ring is flat in the energy space.

To obtain the nodal ring around 3.93 THz, we used the eigenvalues of 1000 $\mathbf{q}$-points around the Γ point as input for model fitting by using the PSO method. The optimal model was obtained by randomly generating 1000 points within the BZ, and the parameters giving the best fit for the model are: $E_0 = 4.100$ THz, $t_1 = -1.243\,\text{THz}\,\text{Å}^2$, $t_2 = -1.500$ THz Å, $t_3 = -6.000\,\text{THz}\,\text{Å}^3$, $t_4 = 0.175$ THz, and $t_5 = -1.055\,\text{THz}\,\text{Å}^2$. Figure 10 shows the comparison between DFT results and $k \cdot p$ bands. The phonon dispersions around the nodal ring at the Γ point were obtained from both DFT calculations (represented by dark-gray lines) and $k \cdot p$

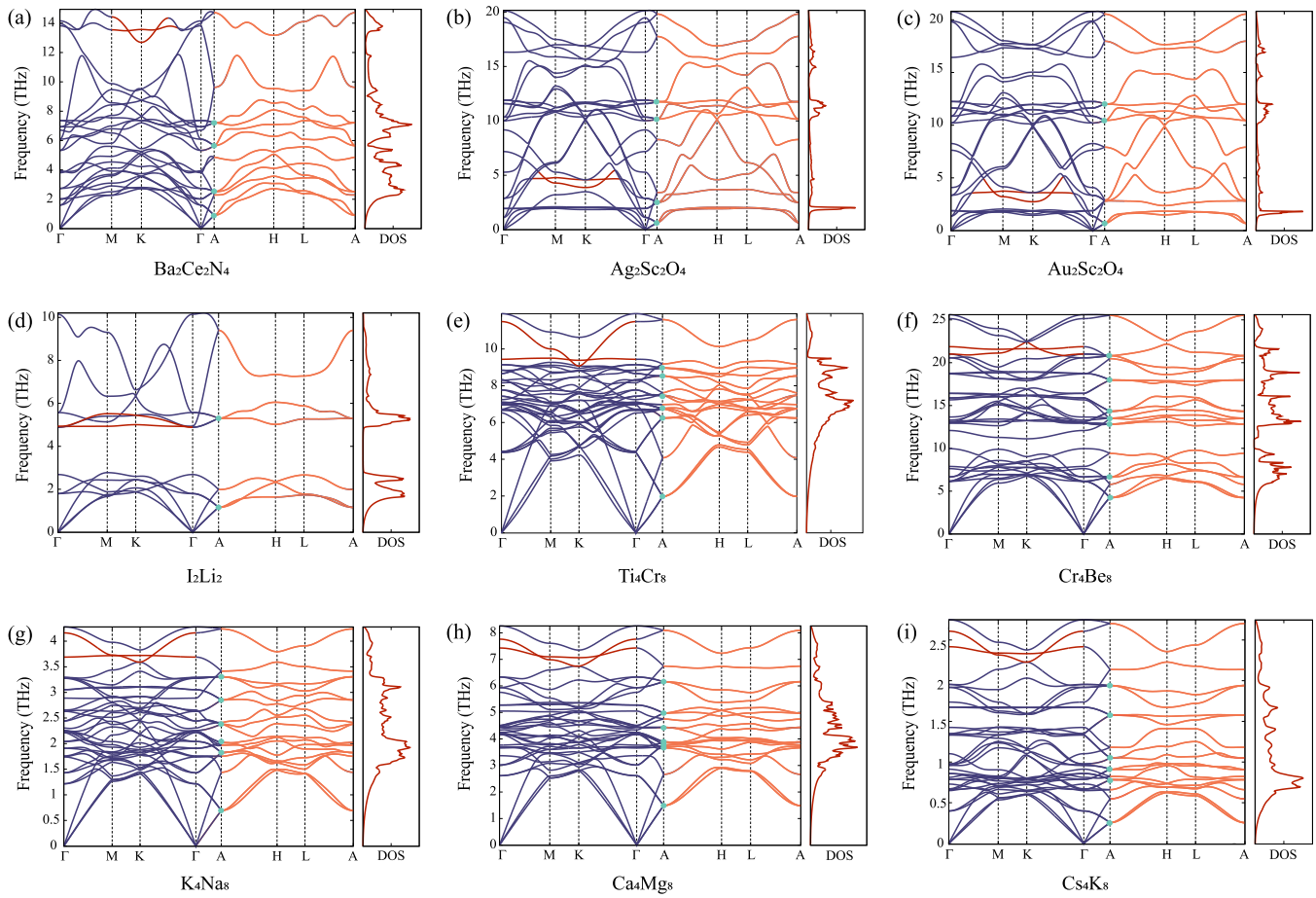

FIG. 14. Phonon dispersion relationships and density of states of all predicted candidate materials that can host quadratic Dirac point, type-III nodal ring, and nodal surface phonons simultaneously. The solid green circles represent quadratic Dirac points, the red lines correspond to the bands forming the type-III nodal ring, and the orange lines are twofold degenerated, indicating the nodal surfaces.

model (represented by red dots). The model results were in good agreement with the DFT results, and the degeneracy feature in the $q_z = 0$ plane was well-reproduced.

To attain a profound understanding of the flat nodal ring, we tuned the parameters of the model to showcase the generation of the type-III nodal ring. Figure 10 shows that our model accurately reproduces the nearly flat band in a wide range of BZ, compared to the DFT results. In this condition, a t_1/t_5 ratio of 1.17 could cause a minor fluctuation in energy. The exact flat band emerged from the eigenvalues of this model when $t_1/t_5 = 1$. As shown in Fig. 11, the fitted parameters were $E_0 = 4.097$ THz, $t_1 = t_5 = -1.200\,\text{THz}\,\text{Å}^2$, $t_2 = -1.500$ THzÅ, $t_3 = -6.000\,\text{THz}\,\text{Å}^3$, and $t_4 = 0.180$ THz. The completely flat band can be seen clearly in the $q_z = 0$ plane where the kinetic energy equals the potential energy.

APPENDIX D: $k \cdot p$ MODEL FOR NODAL SURFACE

In this Appendix, we discuss the derivation of an effective model for the nodal surface. First, we explore $\mathcal{P}$ and $\mathcal{T}$ symmetries, which play similar roles for the nodal ring in SG $P6_3/mmc$. Consequently, the expressions for $h_i(\mathbf{q})$ that satisfy the symmetry requirements share the same formula as Eq. (C4).

However, the nonsymmorphic symmetry $\tilde{M}_z$ has a different matrix representation. From Eqs. (C6) and (C7), we know that the $\tilde{M}_z$ symmetry should anticommute with $\mathcal{I}$, $\{\tilde{M}_z, \mathcal{I}\} = 0$, for $\mathbf{q}$-points on $q_z = \pi$ plane. We further considered other symmetry operations required for the nodal surface. Particularly, the twofold rotation symmetry $C_{2xy} = \{2_{110}|000\}$, which commutes with $\mathcal{I}$, $[C_{2xy}, \mathcal{I}] = 0$. C_{2xy} satisfies the following in the real space:

$$C_{2xy} : (x, y, z) \mapsto (y, x, -z).$$

Combining it with Eq. (C5), we obtained

$$C_{2xy}\tilde{M}_z : (x, y, z) \mapsto (y, x, z - \tfrac{1}{2}),$$
$$\tilde{M}_z C_{2xy} : (x, y, z) \mapsto (y, x, z + \tfrac{1}{2}).$$

Therefore, we found that $C_{2xy}\tilde{M}_z = e^{iq_z \cdot 2\pi}\tilde{M}_z C_{2xy}$. For points on the $q_z = \pi$ plane, C_{2xy} must anticommute with $\tilde{M}_z$, $\{C_{2xy}, \tilde{M}_z\} = 0$.

Based on the relations of $\tilde{M}_z$, C_{2xy}, and $\mathcal{I}$, we chose $\tilde{M}_z$ as σ_1 and C_{2xy} as σ_3 under the parity representation. The C_{2xy} transformation matrix is

$$\begin{bmatrix} 0 & 1 & 0 \\ 1 & 0 & 0 \\ 0 & 0 & -1 \end{bmatrix}.$$

By applying $\tilde{M}_z$ and C_{2xy} operators on the effective model, the final $k \cdot p$ effective Hamiltonian was derived as

$$\mathcal{H}_{\text{eff}}(\mathbf{q}) = t_0\sigma_0 + t_1 q_z \sigma_2. \tag{D1}$$

Our model produced a flat nodal surface on the $q_z = \pi$ plane and a linear dispersion along the q_z direction.

The primitive cell of $BaNa_2$ contains 12 atoms and a total of 36 phonon branches that can be categorized into 18 nodal surfaces. We systematically studied the nodal surface and used the $k \cdot p$ model in Eq. (D1) to fit all phonon branches. The results are summarized in Table II.

To verify the generality of our model, the phonon dispersions for all nodal surfaces at $q_z = \pi$ plane are shown in Fig. 12. Around the A point, the $k \cdot p$ results can fit the DFT results well, both in plane and out of plane. The two bands will degenerate in the plane and split into two independent branches along the right path of the figure. Notably, the dispersions along the q_z direction are linear, and it agrees well with the results from the effective Hamiltonian for QDPs.

APPENDIX E: SURFACE STATES FOR THE QUADRATIC DIRAC POINTS

This Appendix presents the surface states associated with the quadratic Dirac points. As a result of the quadratic Dirac point, the topological phonon surface states can be obtained at the Γ point of the (0001) plane or the Y point of the $(10\bar{1}0)$ plane. Unfortunately, the overlapping with the bulk states makes it challenging to distinguish the surface states. We examined the phonon surface states around the six quadratic Dirac points and illustrated the surface states of the QDP close to 3.396 THz, as shown in Fig. 13.

APPENDIX F: OTHER CANDIDATE MATERIALS

Using our established topological phonon database [25,26], we identified additional candidates that possess quadratic Dirac point, type-III nodal ring, and nodal surface phonons simultaneously. Figure 14 exhibits the phonon bands along high-symmetry lines and the phonon density of states in the whole frequency range for three typical compounds, namely ABC2, AB, and AB2. All of them are dynamically stable phases of SG $P6_3/mmc$ and can be experimentally synthesized. Similar to Fig. 2(c), the quadratic Dirac points are represented by solid green circles. The flat phonon branch forms a type-III nodal ring indicated by the red lines. Along the A-H-L-A path, all orange branches are twofold degenerate, indicating the nodal surface of the $q_z = \pi$ plane.

[1] F. D. M. Haldane, Nobel Lecture: Topological quantum matter, Rev. Mod. Phys. **89**, 040502 (2017).

[2] C.-K. Chiu, J. C. Y. Teo, A. P. Schnyder, and S. Ryu, Classification of topological quantum matter with symmetries, Rev. Mod. Phys. **88**, 035005 (2016).

[3] N. Goldman, J. C. Budich, and P. Zoller, Topological quantum matter with ultracold gases in optical lattices, Nat. Phys. **12**, 639 (2016).

[4] W. Wu, Y. Liu, S. Li, C. Zhong, Z.-M. Yu, X.-L. Sheng, Y. X. Zhao, and S. A. Yang, Nodal surface semimetals: Theory and material realization, Phys. Rev. B **97**, 115125 (2018).

[5] B. Bradlyn, L. Elcoro, J. Cano, M. G. Vergniory, Z. Wang, C. Felser, M. I. Aroyo, and B. A. Bernevig, Topological quantum chemistry, Nature (London) **547**, 298 (2017).

[6] T. Zhang, Y. Jiang, Z. Song, H. Huang, Y. He, Z. Fang, H. Weng, and C. Fang, Catalogue of topological electronic materials, Nature (London) **566**, 475 (2019).

[7] M. G. Vergniory, L. Elcoro, C. Felser, N. Regnault, B. A. Bernevig, and Z. Wang, A complete catalogue of high-quality topological materials, Nature (London) **566**, 480 (2019).

[8] F. Tang, H. C. Po, A. Vishwanath, and X. Wan, Comprehensive search for topological materials using symmetry indicators, Nature (London) **566**, 486 (2019).

[9] M. Konig, S. Wiedmann, C. Brüne, A. Roth, H. Buhmann, L. W. Molenkamp, X.-L. Qi, and S.-C. Zhang, Quantum spin Hall insulator state in HgTe quantum wells, Science **318**, 766 (2007).

[10] D. Hsieh, D. Qian, L. Wray, Y. Xia, Y. S. Hor, R. J. Cava, and M. Z. Hasan, A topological Dirac insulator in a quantum spin Hall phase, Nature (London) **452**, 970 (2008).

[11] Y. Xia, D. Qian, D. Hsieh, L. Wray, A. Pal, H. Lin, A. Bansil, D. Grauer, Y. S. Hor, R. J. Cava, and M. Z. Hasan, Observation of a large-gap topological-insulator class with a single Dirac cone on the surface, Nat. Phys. **5**, 398 (2009).

[12] R.-J. Slager, A. Mesaros, V. Juričić, and J. Zaanen, The space group classification of topological band-insulators, Nat. Phys. **9**, 98 (2013).

[13] S. M. Young, S. Zaheer, J. C. Y. Teo, C. L. Kane, E. J. Mele, and A. M. Rappe, Dirac Semimetal in Three Dimensions, Phys. Rev. Lett. **108**, 140405 (2012).

[14] Z. Wang, Y. Sun, X.-Q. Chen, C. Franchini, G. Xu, H. Weng, X. Dai, and Z. Fang, Dirac semimetal and topological phase transitions in A_3Bi (A = Na, K, Rb), Phys. Rev. B **85**, 195320 (2012).

[15] X. Wan, A. M. Turner, A. Vishwanath, and S. Y. Savrasov, Topological semimetal and Fermi-arc surface states in the electronic structure of pyrochlore iridates, Phys. Rev. B **83**, 205101 (2011).

[16] H. Weng, C. Fang, Z. Fang, B. A. Bernevig, and X. Dai, Weyl Semimetal Phase in Noncentrosymmetric Transition-Metal Monophosphides, Phys. Rev. X **5**, 011029 (2015).

[17] S.-M. Huang, S.-Y. Xu, I. Belopolski, C.-C. Lee, G. Chang, B. Wang, N. Alidoust, G. Bian, M. Neupane, C. Zhang, S. Jia, A. Bansil, H. Lin, and M. Z. Hasan, A Weyl Fermion semimetal with surface Fermi arcs in the transition metal monopnictide TaAs class, Nat. Commun. **6**, 7373 (2015).

[18] R. Li, H. Ma, X. Cheng, S. Wang, D. Li, Z. Zhang, Y. Li, and X.-Q. Chen, Dirac Node Lines in Pure Alkali Earth Metals, Phys. Rev. Lett. **117**, 096401 (2016).

[19] L. M. Schoop, M. N. Ali, C. Straßer, A. Topp, A. Varykhalov, D. Marchenko, V. Duppel, S. S. P. Parkin, B. V. Lotsch, and C. R. Ast, Dirac cone protected by non-symmorphic symmetry

and three-dimensional Dirac line node in ZrSiS, Nat. Commun. **7**, 11696 (2016).

[20] G. Bian, T.-R. Chang, R. Sankar, S.-Y. Xu, H. Zheng, T. Neupert, C.-K. Chiu, S.-M. Huang, G. Chang, I. Belopolski, D. S. Sanchez, M. Neupane, N. Alidoust, C. Liu, B. Wang, C.-C. Lee, H.-T. Jeng, C. Zhang, Z. Yuan, S. Jia *et al.*, Topological nodal-line fermions in spin-orbit metal $PbTaSe_2$, Nat. Commun. **7**, 10556 (2016).

[21] R. Li, J. Li, L. Wang, J. Liu, H. Ma, H.-F. Song, D. Li, Y. Li, and X.-Q. Chen, Underlying Topological Dirac Nodal Line Mechanism of the Anomalously Large Electron-Phonon Coupling Strength on a Be (0001) Surface, Phys. Rev. Lett. **123**, 136802 (2019).

[22] T. Ozawa, H. M. Price, A. Amo, N. Goldman, M. Hafezi, L. Lu, M. C. Rechtsman, D. Schuster, J. Simon, O. Zilberberg, and I. Carusotto, Topological photonics, Rev. Mod. Phys. **91**, 015006 (2019).

[23] Z.-M. Yu, Z. Zhang, G.-B. Liu, W. Wu, X.-P. Li, R.-W. Zhang, S. A. Yang, and Y. Yao, Encyclopedia of emergent particles in three-dimensional crystals, Sci. Bull. **67**, 375 (2022).

[24] Z. Gao and Z. Lan, Flat bands and Z_2 topological phases in a non-Abelian kagome lattice, Phys. Rev. B **102**, 245133 (2020).

[25] J. Li, J. Liu, S. A. Baronett, M. Liu, L. Wang, R. Li, Y. Chen, D. Li, Q. Zhu, and X.-Q. Chen, Computation and data driven discovery of topological phononic materials, Nat. Commun. **12**, 1204 (2021).

[26] X.-Q. Chen, J. Liu, and J. Li, Topological phononic materials: Computation and data, Innovation **2**, 100134 (2021).

[27] Y. Liu, N. Zou, S. Zhao, X. Chen, Y. Xu, and W. Duan, Ubiquitous topological states of phonons in solids: Silicon as a model material, Nano Lett. **22**, 2120 (2022).

[28] J. Wang, H. Yuan, M. Kuang, T. Yang, Z.-M. Yu, Z. Zhang, and X. Wang, Coexistence of zero-, one-, and two-dimensional degeneracy in tetragonal SnO_2 phonons, Phys. Rev. B **104**, L041107 (2021).

[29] C. Xie, Y. Liu, Z. Zhang, F. Zhou, T. Yang, M. Kuang, X. Wang, and G. Zhang, Sixfold degenerate nodal-point phonons: Symmetry analysis and materials realization, Phys. Rev. B **104**, 045148 (2021).

[30] T. Yang, C. Xie, H. Chen, X. Wang, and G. Zhang, Phononic nodal points with quadratic dispersion and multifold degeneracy in the cubic compound Ta_3Sn, Phys. Rev. B **105**, 094310 (2022).

[31] M. Zhong, Y. Liu, F. Zhou, M. Kuang, T. Yang, X. Wang, and G. Zhang, Coexistence of phononic sixfold, fourfold, and threefold excitations in the ternary antimonide $Zr_3Ni_3Sb_4$, Phys. Rev. B **104**, 085118 (2021).

[32] G. Liu, Z. Huang, Z. Chen, Y. Jin, C. He, and H. Xu, Coexistence of charge-2 Dirac and Weyl phonons in chiral space groups, Phys. Rev. B **106**, 054306 (2022).

[33] W.-W. Yu, Y. Liu, L. Tian, T. He, X. Zhang, and G. Liu, Phononic linear and quadratic nodal points in monolayer XH (X=Si, Ge, Sn), J. Phys.: Condens. Matter **34**, 155703 (2022).

[34] J. Li, Q. Xie, S. Ullah, R. Li, H. Ma, D. Li, Y. Li, and X.-Q. Chen, Coexistent three-component and two-component Weyl phonons in TiS, ZrSe, and HfTe, Phys. Rev. B **97**, 054305 (2018).

[35] Q. Xie, J. Li, S. Ullah, R. Li, L. Wang, D. Li, Y. Li, S. Yunoki, and X.-Q. Chen, Phononic Weyl points and one-way topologically protected nontrivial phononic surface arc states in noncentrosymmetric WC-type materials, Phys. Rev. B **99**, 174306 (2019).

[36] T. Zhang, Z. Song, A. Alexandradinata, H. Weng, C. Fang, L. Lu, and Z. Fang, Double-Weyl Phonons in Transition-Metal Monosilicides, Phys. Rev. Lett. **120**, 016401 (2018).

[37] H. Miao, T. T. Zhang, L. Wang, D. Meyers, A. H. Said, Y. L. Wang, Y. G. Shi, H. M. Weng, Z. Fang, and M. P. M. Dean, Observation of Double Weyl Phonons in Parity-Breaking FeSi, Phys. Rev. Lett. **121**, 035302 (2018).

[38] G. Ding, F. Zhou, Z. Zhang, Z.-M. Yu, and X. Wang, Charge-two Weyl phonons with type-III dispersion, Phys. Rev. B **105**, 134303 (2022).

[39] Q.-B. Liu, Z. Wang, and H.-H. Fu, Charge-four Weyl phonons, Phys. Rev. B **103**, L161303 (2021).

[40] P.-F. Liu, J. Li, X.-H. Tu, H. Li, J. Zhang, P. Zhang, Q. Gao, and B.-T. Wang, First-principles prediction of ideal type-II Weyl phonons in wurtzite ZnSe, Phys. Rev. B **103**, 094306 (2021).

[41] T. Zhang, R. Takahashi, C. Fang, and S. Murakami, Twofold quadruple Weyl nodes in chiral cubic crystals, Phys. Rev. B **102**, 125148 (2020).

[42] R. Wang, B. W. Xia, Z. J. Chen, B. B. Zheng, Y. J. Zhao, and H. Xu, Symmetry-Protected Topological Triangular Weyl Complex, Phys. Rev. Lett. **124**, 105303 (2020).

[43] Z. Huang, Z. Chen, B. Zheng, and H. Xu, Three-terminal Weyl complex with double surface arcs in a cubic lattice, npj Comput. Mater. **6**, 87 (2020).

[44] B. W. Xia, R. Wang, Z. J. Chen, Y. J. Zhao, and H. Xu, Symmetry-Protected Ideal Type-II Weyl Phonons in CdTe, Phys. Rev. Lett. **123**, 065501 (2019).

[45] J. Liu, W. Hou, E. Wang, S. Zhang, J.-T. Sun, and S. Meng, Ideal type-II Weyl phonons in wurtzite CuI, Phys. Rev. B **100**, 081204(R) (2019).

[46] Z. J. Chen, R. Wang, B. W. Xia, B. B. Zheng, Y. J. Jin, Y.-J. Zhao, and H. Xu, Three-Dimensional Dirac Phonons with Inversion Symmetry, Phys. Rev. Lett. **126**, 185301 (2021).

[47] Y. Jin, R. Wang, and H. Xu, Recipe for Dirac phonon states with a quantized valley Berry phase in two-dimensional hexagonal lattices, Nano Lett. **18**, 7755 (2018).

[48] T. Yang, Q. Gu, P. Wang, Z. Wu, and Z. Zhang, Phononic quadratic nodal lines of different types in Li_2NaN, Appl. Phys. Lett. **121**, 053102 (2022).

[49] T. T. Zhang, H. Miao, Q. Wang, J. Q. Lin, Y. Cao, G. Fabbris, A. H. Said, X. Liu, H. C. Lei, Z. Fang, H. M. Weng, and M. P. M. Dean, Phononic Helical Nodal Lines with $\mathcal{PT}$ Protection in MoB_2, Phys. Rev. Lett. **123**, 245302 (2019).

[50] G. Ding, T. Sun, G. Surucu, O. Surucu, A. Gencer, and X. Wang, Complex nodal structure phonons formed by open and closed nodal lines in CoAsS and Na_2CuP solids, Phys. Chem. Chem. Phys. **24**, 17210 (2022).

[51] J. Wang, H. Yuan, Z.-M. Yu, Z. Zhang, and X. Wang, Coexistence of symmetry-enforced phononic Dirac nodal-line net and three-nodal surfaces phonons in solid-state materials: Theory and materials realization, Phys. Rev. Mater. **5**, 124203 (2021).

[52] J. Li, Q. Xie, J. Liu, R. Li, M. Liu, L. Wang, D. Li, Y. Li, and X.-Q. Chen, Phononic Weyl nodal straight lines in MgB_2, Phys. Rev. B **101**, 024301 (2020).

[53] G. Liu, Y. Jin, Z. Chen, and H. Xu, Symmetry-enforced straight nodal-line phonons, Phys. Rev. B **104**, 024304 (2021).

[54] Q.-B. Liu, H.-H. Fu, G. Xu, R. Yu, and R. Wu, Categories of phononic topological Weyl open nodal lines and a potential

material candidate: $Rb_2Sn_2O_3$, J. Phys. Chem. Lett. **10**, 4045 (2019).
[55] Y. J. Jin, Z. J. Chen, B. W. Xia, Y. J. Zhao, R. Wang, and H. Xu, Ideal intersecting nodal-ring phonons in bcc C_8, Phys. Rev. B **98**, 220103(R) (2018).
[56] R. Y. Wang, Z. J. Chen, Z. Q. Huang, B. W. Xia, and H. Xu, Classification and materials realization of topologically robust nodal ring phonons, Phys. Rev. Mater. **5**, 084202 (2021).
[57] B. Zheng, B. Xia, R. Wang, Z. Chen, J. Zhao, Y. Zhao, and H. Xu, Ideal type-III nodal-ring phonons, Phys. Rev. B **101**, 100303(R) (2020).
[58] F. Zhou, Z. Zhang, H. Chen, M. Kuang, T. Yang, and X. Wang, Hybrid-type nodal ring phonons and coexistence of higher-order quadratic nodal line phonons in an AgZr alloy, Phys. Rev. B **104**, 174108 (2021).
[59] B. Peng, Y. Hu, S. Murakami, T. Zhang, and B. Monserrat, Topological phonons in oxide perovskites controlled by light, Sci. Adv. **6**, 46 (2020).
[60] J. Li, L. Wang, J. Liu, R. Li, Z. Zhang, and X.-Q. Chen, Topological phonons in graphene, Phys. Rev. B **101**, 081403 (2020).
[61] W. Deng, J. Lu, F. Li, X. Huang, M. Yan, J. Ma, and Z. Liu, Nodal rings and drumhead surface states in phononic crystals, Nat. Commun. **10**, 1769 (2019).
[62] B. Peng, S. Murakami, B. Monserrat, and T. Zhang, Degenerate topological line surface phonons in quasi-1D double helix crystal SnIP, npj Comput. Mater. **7**, 195 (2021).
[63] Z. J. Chen, Z. J. Xie, Y. J. Jin, G. Liu, and H. Xu, Hybrid nodal-ring phonons with hourglass dispersion in $AgAlO_2$, Phys. Rev. Mater. **6**, 034202 (2022).
[64] Q.-B. Liu, H.-H. Fu, and R. Wu, Topological phononic nodal hexahedron net and nodal links in the high-pressure phase of the semiconductor CuCl, Phys. Rev. B **104**, 045409 (2021).
[65] Y. S. Chen, F. F. Huang, P. Zhou, Z. S. Ma, and L. Z. Sun, Ideal topological phononic nodal chain in K_2O materials class, New J. Phys. **23**, 103043 (2021).
[66] F. Zhou, H. Chen, Z.-M. Yu, Z. Zhang, and X. Wang, Realistic cesium fluogermanate: An ideal platform to realize the topologically nodal-box and nodal-chain phonons, Phys. Rev. B **104**, 214310 (2021).
[67] J. Zhu, W. Wu, J. Zhao, H. Chen, L. Zhang, and S. A. Yang, Symmetry-enforced nodal chain phonons, npj Quantum Mater. **7**, 52 (2022).
[68] G. Ding, T. Sun, and X. Wang, Ideal nodal-net, nodal-chain, and nodal-cage phonons in some realistic materials, Phys. Chem. Chem. Phys. **24**, 11175 (2022).
[69] Z. Wang, W. Zhou, A. N. Rudenko, and S. Yuan, Lattice dynamics and topological surface phonon states in cuprous oxide Cu_2O, Phys. Rev. B **103**, 195137 (2021).
[70] M. Wang, Y. Wang, Z. Yang, J. Fan, B. Zheng, R. Wang, and X. Wu, Symmetry-enforced nodal cage phonons in Th_2BC_2, Phys. Rev. B **105**, 174309 (2022).
[71] B. Zheng, F. Zhan, X. Wu, R. Wang, and J. Fan, Hourglass phonons jointly protected by symmorphic and nonsymmorphic symmetries, Phys. Rev. B **104**, L060301 (2021).
[72] X. Wang, F. Zhou, T. Yang, M. Kuang, Z.-M. Yu, and G. Zhang, Symmetry-enforced ideal lanternlike phonons in the ternary nitride Li_6WN_4, Phys. Rev. B **104**, L041104 (2021).
[73] J. Wang, H. Yuan, Y. Liu, F. Zhou, X. Wang, and G. Zhang, Hourglass Weyl and Dirac nodal line phonons, and drumhead-like and torus phonon surface states in orthorhombic-type KCuS, Phys. Chem. Chem. Phys. **24**, 2752 (2022).
[74] Q.-B. Liu, Z.-Q. Wang, and H.-H. Fu, Ideal topological nodal-surface phonons in RbTeAu-family materials, Phys. Rev. B **104**, L041405 (2021).
[75] C. Xie, H. Yuan, Y. Liu, and X. Wang, Two-nodal surface phonons in solid-state materials, Phys. Rev. B **105**, 054307 (2022).
[76] C. Xie, H. Yuan, Y. Liu, X. Wang, and G. Zhang, Three-nodal surface phonons in solid-state materials: Theory and material realization, Phys. Rev. B **104**, 134303 (2021).
[77] W. Kohn and J. M. Luttinger, Theory of donor states in silicon, Phys. Rev. **98**, 915 (1955).
[78] J. M. Luttinger, Quantum theory of cyclotron resonance in semiconductors: General theory, Phys. Rev. **102**, 1030 (1956).
[79] T. B. Bahder, Eight-band $k \cdot p$ model of strained zinc-blende crystals, Phys. Rev. B **41**, 11992 (1990).
[80] A. P. Schnyder, S. Ryu, A. Furusaki, and A. W. W. Ludwig, Classification of topological insulators and superconductors in three spatial dimensions, Phys. Rev. B **78**, 195125 (2008).
[81] S. Li, Z.-M. Yu, Y. Liu, S. Guan, S.-S. Wang, X. Zhang, Y. Yao, and S. A. Yang, Type-II nodal loops: Theory and material realization, Phys. Rev. B **96**, 081106(R) (2017).
[82] G. Kresse and J. Hafner, *Ab initio* molecular dynamics for liquid metals, Phys. Rev. B **47**, 558 (1993).
[83] G. Kresse and J. Hafner, *Ab initio* molecular-dynamics simulation of the liquid-metal–amorphous-semiconductor transition in germanium, Phys. Rev. B **49**, 14251 (1994).
[84] G. Kresse and J. Furthmüller, Efficiency of *ab initio* total energy calculations for metals and semiconductors using a plane-wave basis set, Comput. Mater. Sci. **6**, 15 (1996).
[85] P. Hohenberg and W. Kohn, Inhomogeneous electron gas, Phys. Rev. **136**, B864 (1964).
[86] W. Kohn and L. J. Sham, Self-consistent equations including exchange and correlation effects, Phys. Rev. **140**, A1133 (1965).
[87] P. E. Blöchl, Projector augmented-wave method, Phys. Rev. B **50**, 17953 (1994).
[88] G. Kresse and D. Joubert, From ultrasoft pseudopotentials to the projector augmented-wave method, Phys. Rev. B **59**, 1758 (1999).
[89] J. P. Perdew, K. Burke, and M. Ernzerhof, Generalized Gradient Approximation Made Simple, Phys. Rev. Lett. **77**, 3865 (1996).
[90] L. Chaput, A. Togo, I. Tanaka, and G. Hug, Phonon-phonon interactions in transition metals, Phys. Rev. B **84**, 094302 (2011).
[91] A. Togo and I. Tanaka, First principles phonon calculations in materials science, Scr. Mater. **108**, 1 (2015).
[92] S. Baroni, S. de Gironcoli, A. Dal Corso, and P. Giannozzi, Phonons and related crystal properties from density-functional perturbation theory, Rev. Mod. Phys. **73**, 515 (2001).
[93] M. P. L. Sancho, J. M. L. Sancho, J. M. L. Sancho, and J. Rubio, Highly convergent schemes for the calculation of bulk and surface Green functions, J. Phys. F: Met. Phys. **15**, 851 (1985).
[94] G. J. Snyder and A. Simon, The new laves phase Na_2Ba, Z. Naturforsch. B **49**, 189 (1994).
[95] C. Bradley and A. Cracknell, *The Mathematical Theory of Symmetry in Solids: Representation Theory for Point Groups and Space Groups* (Oxford University Press, Oxford, UK, 2009).